UNIVERSITÀ DEGLI STUDI DI PADOVA

SCUOLA DI SCIENZE
Dipartimento di Geoscienze

TESI DI LAUREA MAGISTRALE IN GEOPHYSICS FOR NATURAL RISKS AND RESOURCES

FIRST IDENTIFICATION AND CHARACTERIZATION OF LONG-PERIOD EARTHQUAKES IN THE LARDERELLO-TRAVALE GEOTHERMAL FIELD

Relatore: Prof. Piero Poli
Correlatore: Prof. Giulio Di Toro

Laureanda: Chulalak Sundod
Matricola: 2081010

ANNO ACCADEMICO 2023-2024

Dedicated

Table of Contents

Abstract

Determining and characterising seismic activity in geothermal fields is crucial for understanding the dynamic behaviour and associated risks of these uniquely volatile regions. The present study of the Larderello-Travale Geothermal field in Tuscany represents the first ever documented identification and comprehensive analysis of long-period, low-frequency seismic signals in Italy.

The research utilises seismic waveform data captured by a TRIF seismic station located at the heart of the Larderello-Travale area with the magnitudes ranging from -1.0 local magnitude (ML) recorded between January 2011 and April 2024. Employing frequency index analysis by calculating the ratio of low-frequency and high-frequency of the waveforms, the study quantifies the relative dominance of low-frequency components of seismic signals. An estimation of the stress drop was then calculated by employing spectra modelling for long-period earthquake events.

The aim was to identify long-period earthquake events that are distinct from regular earthquake signals and often associated with unique subsurface mechanisms, such as the slow movement of fluids and magma in the shallow crust and tectonic processes in the deep crust. From over 1500 seismic events detected by the TRIF, I identified 13 long-period earthquakes utilising a frequency index threshold of 1.25. Remarkably, spectral fitting techniques revealed the identified long-period earthquakes possess significantly lower corner frequencies and stress drops compared to the global range for typical earthquakes.

These findings enhance our understanding of the complex seismic activities of the Larderello-Travale Geothermal field. This emerging knowledge should inform the development of more effective monitoring and management strategies, contributing to the sustainable production of geothermal energy.

Riassunto

La determinazione e la caratterizzazione dell'attività sismica nei campi geotermici è fondamentale per comprendere il comportamento dinamico e i rischi associati di queste regioni uniche e volatili. Il presente studio sul campo geotermico di Larderello-Travale, in Toscana, rappresenta la prima identificazione documentata e l'analisi completa di segnali sismici di lungo periodo e a bassa frequenza in Italia.

La ricerca utilizza i dati della forma d'onda sismica acquisiti da una stazione sismica TRIF situata nel cuore dell'area di Larderello-Travale, con magnitudo comprese tra -1,0 magnitudo locale (ML) e registrate tra gennaio 2011 e aprile 2024. Utilizzando l'analisi dell'indice di frequenza (FI), calcolando il rapporto tra le forme d'onda a bassa e ad alta frequenza, lo studio quantifica la dominanza relativa delle componenti a bassa frequenza dei segnali sismici. Una stima della caduta di stress è stata poi calcolata utilizzando la modellazione degli spettri per eventi sismici di lunga durata.

L'obiettivo era quello di identificare gli eventi sismici di lungo periodo che sono distinti dai segnali sismici regolari e spesso associati a meccanismi unici del sottosuolo, come il lento movimento di fluidi e magma nella crosta superficiale e i processi tettonici nella crosta profonda. Da oltre 1500 eventi sismici rilevati dal TRIF, ho identificato 13 terremoti di lungo periodo utilizzando una soglia di indice di frequenza di 1,25. Le tecniche di adattamento spettrale hanno rivelato che i terremoti a lungo periodo identificati possiedono frequenze angolari e cadute di stress significativamente più basse rispetto alla gamma globale dei terremoti tipici.

Questi risultati migliorano la nostra comprensione della complessa attività sismica del campo geotermico di Larderello-Travale. Queste conoscenze emergenti dovrebbero informare lo sviluppo di strategie di monitoraggio e

gestione più efficaci, contribuendo alla produzione sostenibile di energia geotermica.

Chapter 1

Introduction

Geothermal energy is widely recognised as a sustainable source of electricity globally. It utilises hot water or steam extracted from deep within the Earth's crust to drive turbines to generate electricity (Fridleifsson et al., 2008). Geothermal fields are typically situated in naturally hot regions of the Earth's crust, necessitating the injection of water into these subsurface areas in the process to harness energy. Despite its environmental benefits, geothermal energy faces significant challenges related to seismic activity within its operational areas.

Seismic activities can arise from various causes such as subsurface ruptures (Bolt, 2024) or fluid movements induced by geological structures or during geothermal production (e.g., Ward, 1972; Jousset et al., 2010). The induced seismicity from the operation of geothermal power plants has the potential to impact local communities, inconvenience building residents, cause damage to infrastructure, and affect the environment as well as the geothermal power plant itself (Zastrow, 2019). For example, in 2017, a significant earthquake measuring 5.4 magnitude led to the closure of a geothermal power plant in Pohang City, South Korea (Ellsworth et al., 2019; Zastrow, 2019). Similarly, operations at a local geothermal power plant in Basel, Switzerland, were affected by a 3.2 magnitude earthquake on December 8, 2006 (Mignan et al., 2015).

Identifying long-period earthquakes is crucial for understanding and mitigating the seismic risks associated with geothermal energy extraction. These earthquakes are key indicators of fluid movements within the subsurface, influenced by both natural processes and geothermal activities. Investigating

them in geothermal areas is essential for determining if geothermal activities can induce seismicity and for gaining insights into fluid dynamics within the reservoir.

This thesis focuses on analysing seismic signals within the Larderello-Travale geothermal field in Tuscany, Italy, specifically aiming to identify previously unrecognized long-period earthquakes. These findings highlight the complex interaction between geological factors and extraction activities in geothermal energy production. Enhancing our understanding of the geophysical processes driving seismicity in geothermal fields is crucial for developing strategies to mitigate risks and optimize the sustainable utilization of geothermal resources.

1.1 Objective

The primary objective of this study is to identify, characterize, and understand long-period earthquakes within the Larderello-Travale geothermal field. Long-period earthquakes serve as crucial indicators of fluid movement within geothermal reservoirs. By analysing these seismic signals, this research aims to enhance our understanding of the complex geological dynamics underlying geothermal energy extraction. Specifically, the study aims to achieve the following objectives:

- Utilise frequency index (FI) analysis to distinguish long-period earthquakes from typical seismic events.
- Estimate stress drop values for the identified long-period earthquakes using spectral fitting techniques.
- Investigate the spatial and depth distribution of these long-period earthquakes, particularly in relation to geothermal features.
- Explore the potential influence of geothermal operations, such as fluid extraction and injection, on seismic activity in the area.

1.2 Study area

The Larderello-Travale Geothermal Field, located in the western part of Tuscany, Italy, is recognized as the world's oldest geothermal power field (Saccorotti et al., 2014). The Larderello-Travale geothermal field spans a significant area in the Northern Apennines (Saccorotti et al., 2014). Larderello and Travale, situated about 15 km apart, share comparable geological features: they both have a shallow carbonate reservoir that has been utilised for an extended period, as well as a deeper reservoir within the metamorphic basement, which was identified within the past two decades (Bertani et al., 2005). Since the Pliocene, shallow-level intrusions have formed widespread areas of intense heat and connected hydrothermal systems. These systems have been extensively studied through various wells drilled for geothermal exploration and exploitation (see, for example: Gianelli, Manzella, & Puxeddu, 1997; Carella et al., 2000; Gianelli & Ruggieri, 2002; Musumeci et al., 2002).

1.2.1 Geological setting

In the Larderello-Travale area, three main regional tectonostratigraphic elements are present (Batini et al., 2003) (figure 1.1):

- Neogene and quaternary deposits: These deposits date from the late Miocene to the Pliocene and Quaternary periods. They consist of continental to marine sediments filling the extensional tectonic depressions and unconformably overlie the pre-Neogene substratum.
- The Ligurian complex: This complex includes the Ligurian units and the sub-Ligurian unit, composed of remnants of the Jurassic oceanic basement and its pelagic sedimentary cover. The Ligurian complex was thrust eastwards over the Tuscan domain during the latest Oligocene to early Miocene times.
- The Tuscan unit (Tuscan Nappe): This unit relates to the late Triassic-early Miocene sedimentary cover of the Adria continental Plaeomargin. It was detached from its substratum along the Triassic evaporite level and was

thrust over the outer palaeogeographical domains during late Oligocene-early Miocene compression.

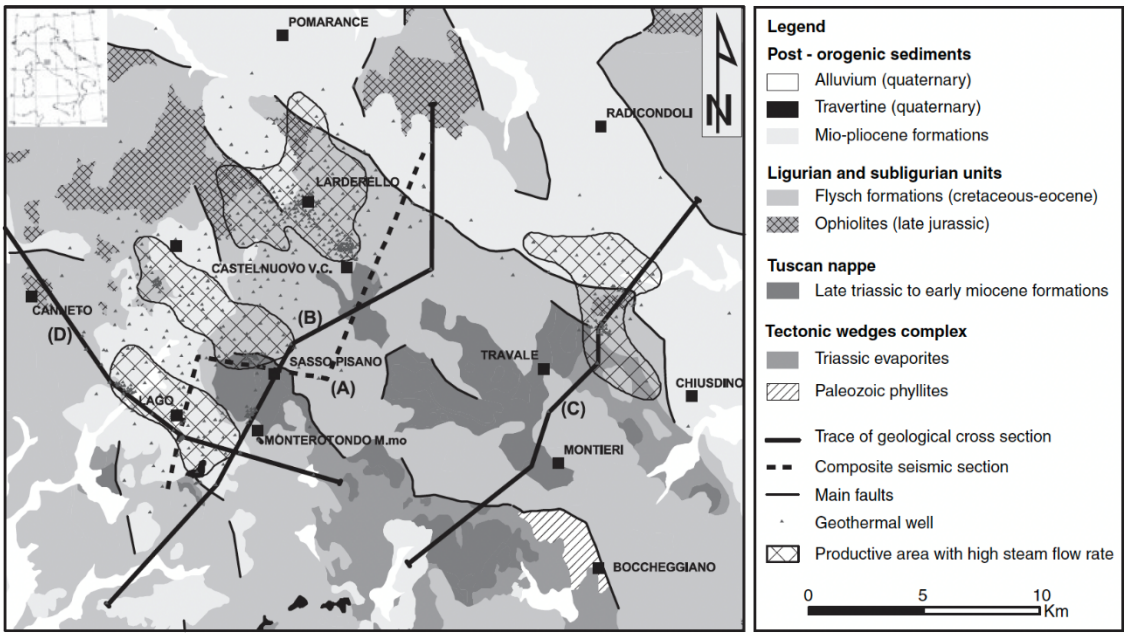

Figure 1.1 Geological and geothermal characteristics sketch map of the Larderello-Travale geothermal area (adapted by Bertini et al. 2006 after Lazzarotto et al., 2002 a, b).

Beneath these elements lies the Tuscan Metamorphic complex (figure 1.2), mainly known through geothermal drilling that penetrates down to about 4.5 km. This complex comprises two metamorphic units:

Monticiano-Roccastrada Unit (figure 1.2):

- Verrucano Group: Comprising Carnian phyllites and metacarbonates (marine littoral facies) and middle-early Triassic continental quartzites and quartz conglomerates.
- Phyllite-Quartzite group: Consisting mainly of Palaeozoic phyllites and quartzites, with layers of anhydritic dolomites and basic metavolcanites. It shows Alpine greenschist metamorphism over a previous Hercynian metamorphism.

- Micaschist Group: Containing Palaeozoic rocks like garnet-bearing micaschists and quartzites with amphibolite zones, affected by Alpine and Hercynian deformations. The micaschists were particularly affected by a synkinematic Hercynian metamorphism and an early Permian thermal event (Del Moro et al., 1982; Pandeli et al., 1994 and references therein).

Gneiss Complex (Figure 1.2): This complex features pre-Alpine polymetamorphic gneiss and paragneiss with amphibolite and orthogneiss intercalations. Unlike the Monticiano-Roccastrada unit, it does not record the Alpine orogeny (Elter and Pandeli, 1990). Deep boreholes have encountered granitoids and felsic dykes at various depths, dated to 3.8–2.25 Ma (Villa & Puxeddu, 1994; Gianelli and Laurenzi, 2001).

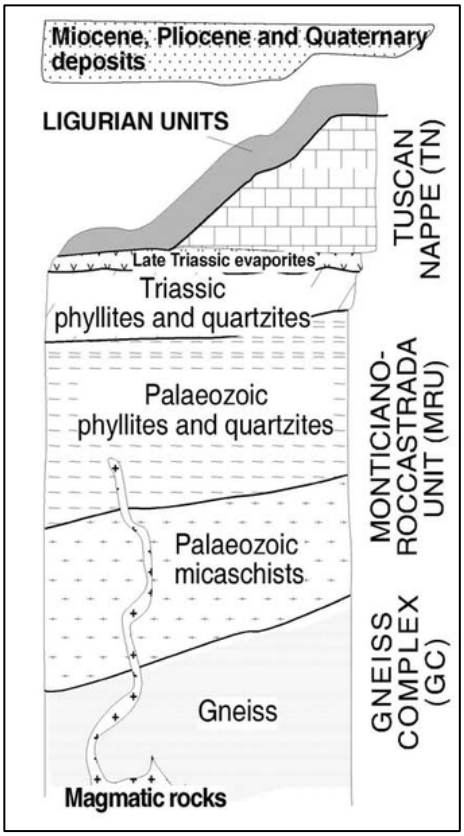

Figure 1.2 Tectonostratigraphic units in the Larderello geothermal area (adapted by Brogi et al., 2012 after Batini et al. 2003).

Figure 1.1 illustrates the primary fault lines in the region. The geological stack has been disrupted by a series of extensional faults ranging from low to high angles since the Miocene period (Decandia et al., 2001). The main faults in the Larderello geothermal fields are predominantly normal faults associated with the latest extensional activity, which has persisted since the late Pliocene period. These faults mainly affect the shallow layers of the crust, approximately 1 km deep, and include notable north-west trending faults, north-east dipping faults, and steeply dipping north-east trending faults with strike-slip characteristics (Brogi et al., 2003).

1.2.2 Larderello-Travale geothermal production

The Larderello-Travale geothermal field produces high enthalpy geothermal fluids with temperatures ranging from 150-260°C and pressures between 2–15 bar. Figure 1.3 illustrates the heat flow contour of the geothermal area. These fluids mainly consist of superheated steam and minor gases (Batini et al., 2003). The generation of superheated steam at Larderello-Travale is primarily driven by substantial heat transfer from the surrounding rocks to the fluid (Minissale, 1991). As of 2007, the Larderello geothermal field contributed 632 MWe to Italy's total geothermal capacity of 711 MWe (Bertani, 2007; Buonasorte et al., 2007).

Initially, hot steam was extracted from a shallow reservoir composed of Mesozoic carbonate-anhydrite formations at depths of 500-1500 metres. However, since the 1980s, extraction has extended to a deeper reservoir exceeding 3000 meters, located within metamorphic rocks. The consistent pressure and composition of the geothermal fluid across a drilled area of about 400 km² suggests a large reservoir characterized by fracture permeability (Bertani et al., 2005; Bertini et al., 2006). The distribution of geothermal wells in the Larderello and Travale areas is shown in figure 1.1. In these fields, well depths typically range from approximately 1000 to 4000 metres. Arias et al. (2010) document a total of 13 deep wells and numerous shallow wells within the

Larderello-Travale system. Currently, about 230 production wells are active at the Larderello-Travale geothermal field, extracting hot steam (Bagagli et al., 2020).

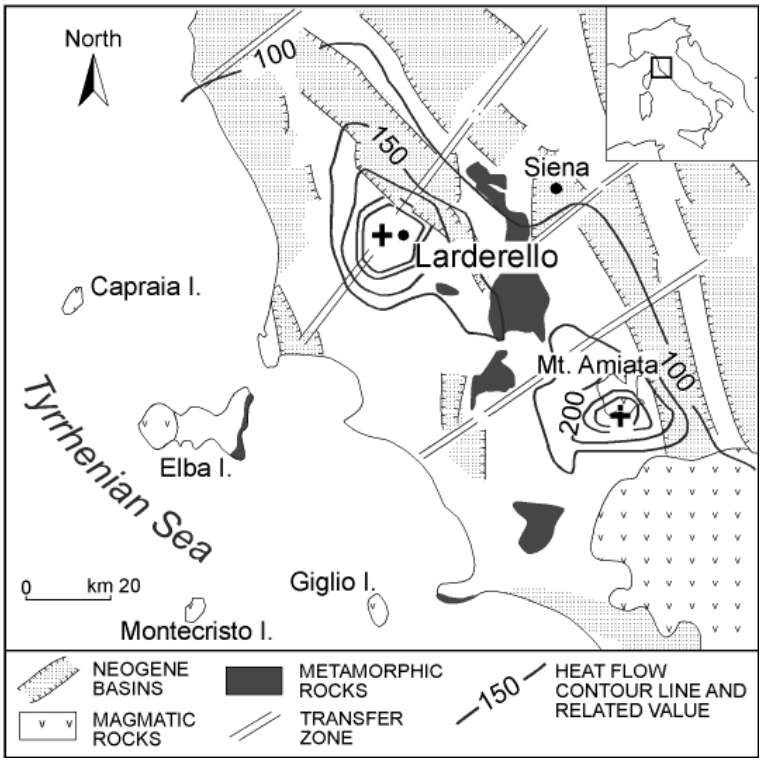

Figure 1.3 Structural sketch map of southern Tuscany with the regional heat flow contour lines (after Baldi et al., 1995).

1.3 Seismic activity in the study area

The elastic strain energy stored in the rocks is released through earthquakes, which happens when the built-up stress overcomes the strength of existing faults (Reid, 1910; Scholz, 1990). Natural earthquakes occur when this stress reaches a tipping point. Human-induced earthquakes are similar but occur when stress or fault strength is altered by human activities (Trifu, 2002).

Induced seismicity has been observed in geothermal regions worldwide, including, for example, in Indonesia (Silitonga et al., 2005; Mulyadi, 2010), Kenya (Simiyu, 1999), and across North and South America (Henderson et al., 2002;

Yamabe and Hamza, 1996), as well as in New Zealand (Hunt and Latter, 1982) for over 40 years. In Europe, Evans et al. (2012) conducted a comprehensive survey outlining induced seismicity responses to fluid injection in European geothermal and CO_2 reservoirs. Each year, the operation of geothermal fields results in thousands of seismic occurrences, although the majority register below a local magnitude of 2 (Evans et al., 2012).

There is ongoing debate egarding whether the characteristics of human-induced earthquakes are different from natural earthquakes. One important subject of discussion is comparing the stress drops between these two types of earthquakes. Huang et al. (2017) studied the stress drops of both types of earthquakes across various research areas, finding no systematic difference between them. This finding is supported by other studies (e.g., Wu et al., 2018; Holmgren et al., 2019; Chu & Sheng, 2023) which observed similar stress drop levels and self-similar relationships in induced earthquakes in Oklahoma, USA, Western Canada, and Sichuan, China. Conversely, studies such as Agurto-Detzel et al. (2017) reported lower absolute stress drops of <1 MPa for induced earthquakes in southeastern Brazil, while Klinger & Werner (2022) noted non-self-similarity in induced earthquakes. Goertz-Allmann et al. (2011) observed varied stress drop levels by location, with lower stress drops near injection sites compared to farther away, which is a pattern consistent with earthquake migration accompanied by fluid migration.

The Larderello-Travale geothermal area has experienced numerous seismic events over the years, the Istituto Nazionale di Geofisica e Vulcanologia (INGV) reporting seismicity rates of up to 10 earthquakes per month over the last 13 years, with a maximum local magnitude of 3.8 (data retrieved in April 2024). Historical records indicate that damaging earthquakes occurred in the Larderello-Travale geothermal area before geothermal exploitation began. For instance, the Travale earthquake with the estimated magnitude of 5.4 and a maximum intensity of 7-8 on the Mercalli-Cancani-Sieberg scale occured in 1724 (Rovida et al., 2016). Batini et al. (1983) found a direct association between the occurrence of

earthquakes and the volume of wastewater injected into the subsurface. Despite this observation, they noted that neither the highest magnitude of earthquake nor the frequency of events exceeding magnitude 2 showed any significant correlation with the reinjection process. Additionally, they noted that a majority of earthquake epicentres were located near operational wells.

1.4 Long-period earthquakes

Long-period earthquakes are a distinct category of seismic events known for their extended durations and unique frequency characteristics. Despite their small magnitudes, they are notable for their low-frequency content (1-8 Hz), which is observed in association with both volcanic and tectonic processes (Farge et al., 2020).

The exact mechanisms behind long-period earthquakes vary globally, and there is no single agreed-upon explanation (Chouet et al., 2003). Fujita and Ida (2003) argue that long-period events signify the movement of volcanic fluids such as magma, water layers, and sills. These seismic events are also considered indicative of degassing processes occurring within specific volcanic or geothermal regions, although do not necessarily signal an impending volcanic eruption (Pitt & Hill, 1994). Tectonic long-period earthquakes have been documented in diverse settings, including subduction zones (e.g., Bostock et al., 2012; Frank et al., 2013; Shelly et al., 2006) and strike-slip plate boundaries (e.g., Chamberlain et al., 2014; Shelly & Hardebeck, 2010). Typically occurring in transitional zones just below the regular seismogenic portions of faults, these events are often associated with areas characterized by low shear wave velocity, high $\frac{V_p}{V_s}$ ratio, indicative of fluid-rich environments (Audet et al., 2009; Bostock et al., 2012; Shelly et al., 2006).

Long-period earthquakes provide valuable insights into subsurface fluid dynamics within volcanic systems, revealing processes that are otherwise hidden (e.g., Frank et al., 2018). Some studies have defined long-period earthquakes in

the context of geothermal fields. For instance, Jousset et al. (2010) observed long-period earthquakes near exploitation wells in the Hengill Geothermal Volcanic Complex, Iceland. The research team suggested these seismic events could be linked to changes in pressure around the wells, resulting from fluctuations in the extraction rate of geothermal fluids.

To characterise long-period earthquakes and gain insights into the complex interactions between geological structures and the extraction of geothermal fluids, several key steps are involved. Waveforms recorded at local seismic stations are analysed for prolonged seismic signals with characteristic low-frequency components. For instance, Figure 1.4 depicts a possible long-period earthquake waveform and its spectrogram recorded in Yellowstone on August 26, 2021, near Norris Geyser Basin. The bottom panel of the figure shows the spectrogram with energy concentrated in the 1–3 Hz range and lasting for approximately 15 seconds (USGS, June 27, 2024). These signals are distinct from typical tectonic or volcanic events shown in Figure 1.5, where the spectrogram displays energy ranging from 1-15 Hz and lasts for approximately 5 seconds (USGS, June 27, 2024).

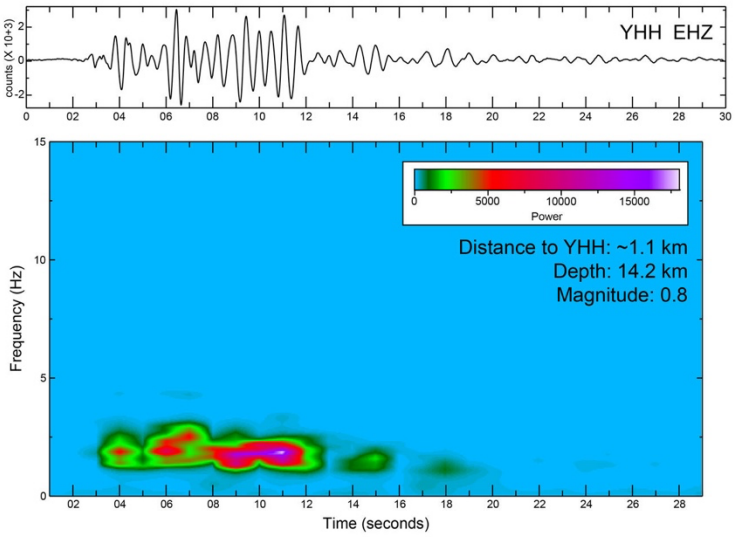

Figure 1.4. Long-period earthquake in Yellowstone that occurred on August 26, 2021, near Norris Geyser Basin. Retrieved from USGS, June 27, 2024.

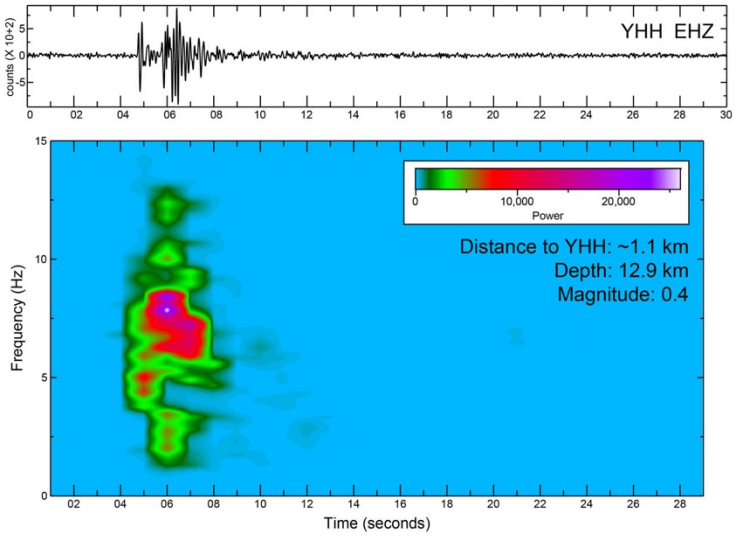

Figure 1.5. Typical volcano-tectonic earthquake occurred near Norris Geyser Basin recorded on August 26, 2021. Retrieved from USGS, June 27, 2024.

In summary, this thesis focuses on identifying and characterizing long-period earthquakes that may be influenced by both natural geological processes and human-induced activities within the Larderello-Travale geothermal field. The following chapters will explore the methods employed for analysis, the main findings, and discuss their implications to enhance our understanding of long-period earthquakes.

Chapter 2

Methodology

2.1 Earthquake catalog

To study the seismicity in the Larderello-Travale geothermal field, seismic data recorded at the TRIF (Trifonti) seismic station was utilised. This station is situated in the middle of the geothermal field area at a latitude of 43.11478°N and longitude of 10.90265°E, with an elevation of 596 metres (see Figure 2.1). Initially, the station was equipped with broadband instruments (HHE, HHN, HHZ) operating from May 2010 to April 2018 at a sample rate of 125 Hz, the TRIF station later transitioned to instruments (CHE, CHN, CHZ) operating at a sample rate of 250 Hz.

Earthquake waveforms were downloaded using the earthquake catalog from Istituto Nazionale di Geofisica e Vulcanologia (INGV, 2005), known for its extensive and accurate seismic records in Italy and surrounding regions. The catalog downloaded covers seismic events from January 2011 to April 2024. An essential dataset for this analysis, the earthquake catalogue is produced by seismic networks and provides a comprehensive record of seismic events. It includes information on the hypocentre, such as its latitude, longitude, and depth, as well as the local magnitude of the earthquake.

The catalog covers seismic events within the geographical boundaries of the Larderello-Travale geothermal field, specifically between latitudes 42.8°N and 43.3°N and longitudes 10.4°E and 11.3°E, ensuring relevance to the study area. Earthquake events with local magnitudes (M_L) ranging from -0.1 were considered, providing a comprehensive analysis of seismic activities.

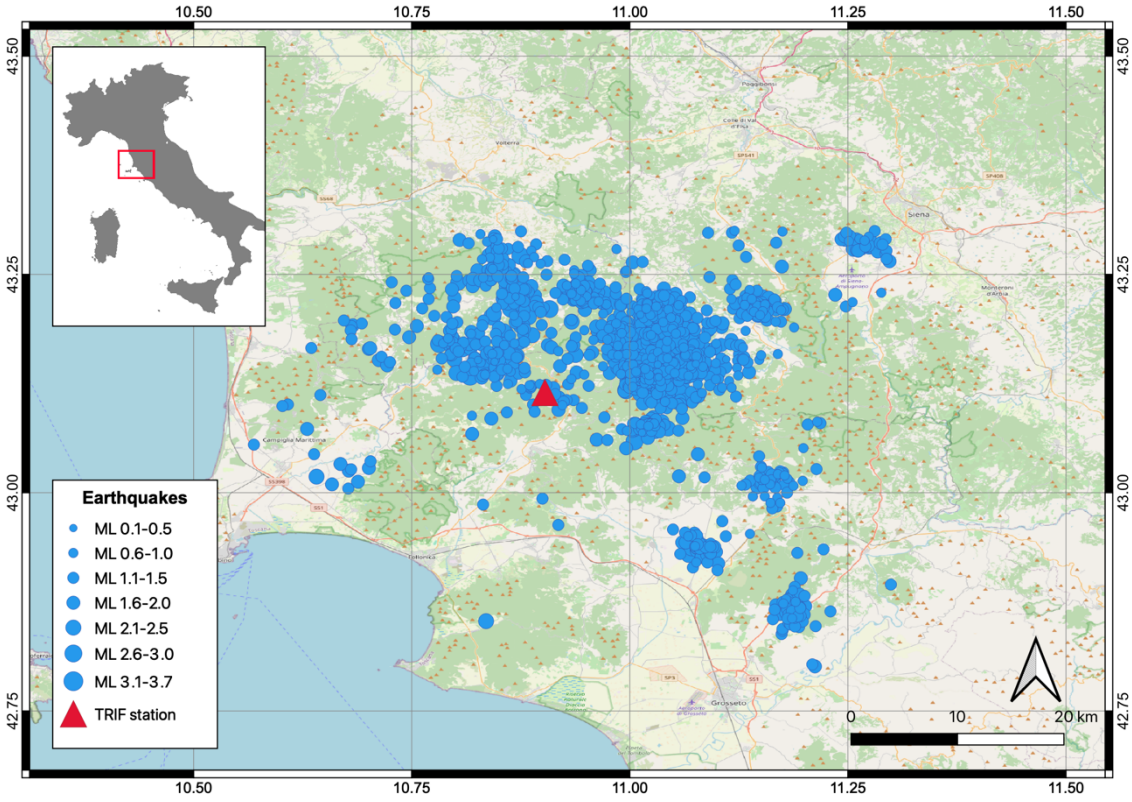

Figure 2.1 Map illustrating the study area and earthquakes downloaded from the earthquake catalog. The red triangle represents the location of the TRIF seismic station. Blue circles indicate earthquake locations.

The final earthquake catalog, derived from seismic events detected by the TRIF station, consists of 1,577 events. Detailed information such as event time, channel, latitude, longitude, depth, and local magnitude is provided for each event. The earthquake data was downloaded in Excel format from the INGV website and processed with specific restrictions to ensure the acquisition of relevant and reliable data. These restrictions, defined within a Python script, include time range specifications, channel priorities, and data completeness thresholds, ensuring the reliability of the seismic dataset for subsequent analysis.

2.2 Frequency index

The frequency content of seismic signals is crucial for understanding the underlying mechanisms of earthquakes. The dominant frequency, representing the peak amplitude in the Fourier spectrum serves as a key parameter for evaluating spectral characteristics. In seismic research, dominant frequency has been utilised to classify waveform types such as low-frequency waveform (e.g., Latter, 1980; McNutt, 2002), providing valuable insights into earthquake source processes. These events can originate from the movement of fluids, such as magma or water, or from slow tectonic shifts within the subsurface (Frank et al., 2018). According to Song, Tan, and Roman (2023), earthquakes rich in high-frequency content are typically associated with volcanic-tectonic events, whereas long-period earthquakes predominantly generate low-frequency energy in the range of 1 to 5 Hz.

In the study of the Larderello-Travale geothermal field, the frequency index is utilised to analyse seismic signals within the region. This index serves as a quantitative measure for identifying long-period events by comparing the spectral amplitudes across different frequency bands (Buurman and West, 2010; Matoza et al., 2014).

Spectral amplitude analysis is a fundamental technique providing insights into the frequency content and energy distribution of seismic signals. It involves decomposing a time series signal into its frequency components using Fourier analysis (Shearer, 2009). To obtain the spectra, I utilised the Fast Fourier Transform (FFT) function provided by the NumPy package in Python. After applying the FFT, the frequency index was calculated. Initially proposed by Buurman and West (2010) and further clarified by Matoza et al. (2014), the frequency index was defined as: $\mathrm{FI} = \log_{10} \frac{\mathrm{A_{Upper}}}{\mathrm{A_{Lower}}}$. In this study, the definition has been adapted to:

$$\mathrm{FI} = \frac{\mathrm{A_{Lower}}}{\mathrm{A_{Upper}}} \tag{2.1}$$

Where $\mathrm{A_{Lower}}$ and $\mathrm{A_{Upper}}$ represent the sum of low-frequency amplitudes and sum of high-frequency amplitudes, respectively. In this study, I selected the frequency bands of 1–5 Hz and 5–10 Hz for $\mathrm{A_{Lower}}$ and $\mathrm{A_{Upper}}$, respectively, following Buurman and West's (2010) method for defining bandwidth of interest. Buurman and West (2010) established these ranges by compiling a set of calibration waveforms. Using standard yet subjective visual criteria, they selected high-quality examples of three earthquake types: canonical high-frequency, low-frequency, and hybrid volcanic events. These selections guided my determination of the frequency bands for the analysis.

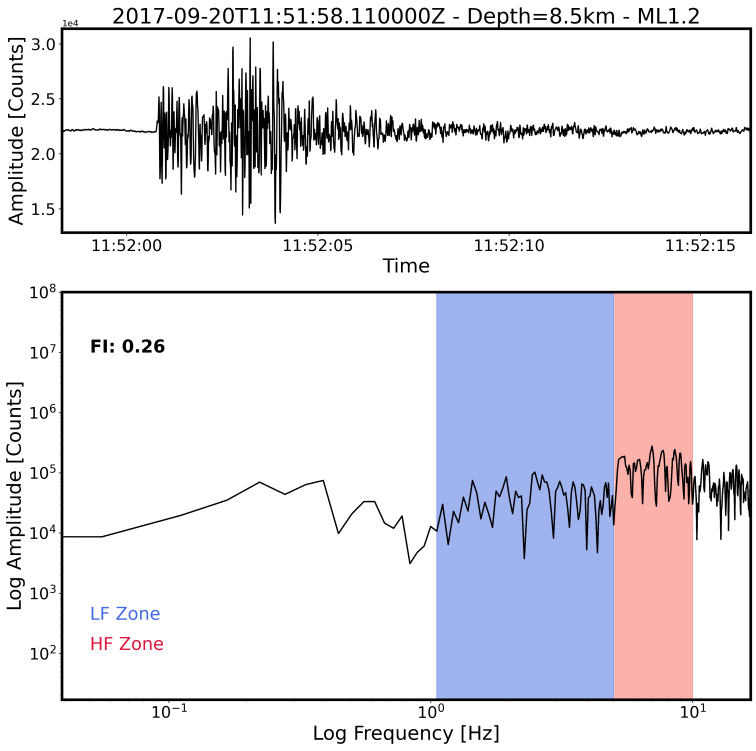

Figure 2.2 Example of a waveform and its amplitude spectra of an earthquake with frequency index values less than 1.25, represent high frequency earthquakes.

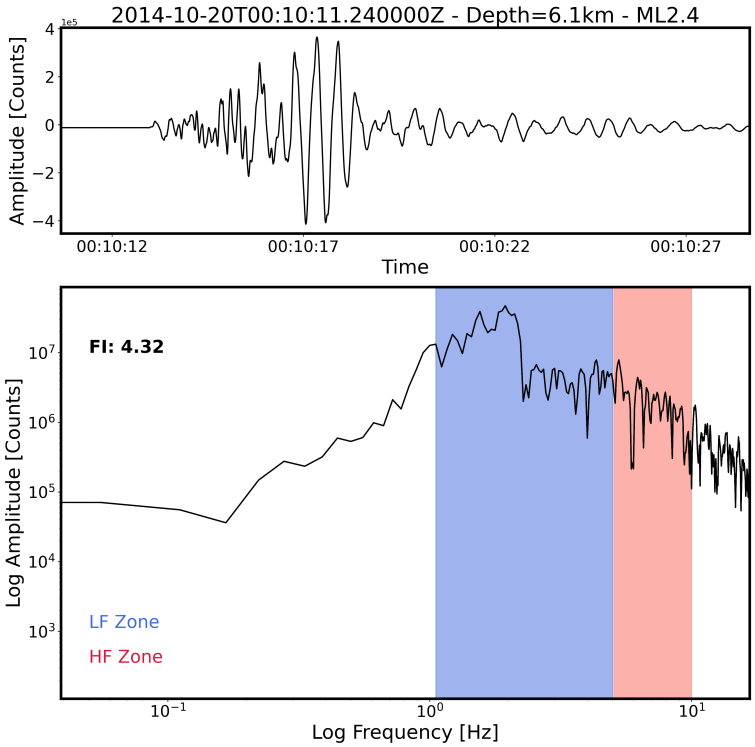

Figure 2.3 Example of a waveform and its amplitude spectra of an earthquake with frequency index values greater than 1.25, represent low frequency earthquakes.

To calculate the frequency index, the mean spectral amplitudes within the defined frequency bands are averaged and analysed. To ensure the comprehensive coverage of earthquake events, the signal was trimmed two seconds before the p-wave arrival and the analysis is extended 18 seconds after, covering the entirety of the seismic waveform (refer to Figure 2.2 and Figure 2.3).

The frequency index provides a relative measure of the spectral energy distribution between these bands. A frequency index value greater than 1.25 indicates that the mean spectral amplitude in the lower frequency band (1–5 Hz) is higher than that in the upper frequency band (5–10 Hz). This observation typically indicates the presence of low-frequency waveforms characteristic of seismic events. Conversely, a frequency index value falling below 1.25 indicates that the mean spectral amplitude in the upper frequency band (5–10 Hz) is higher

than that in the lower frequency band (1–5 Hz), suggesting that high-frequency events dominate (see Figure 2.2 and Figure 2.3).

2.3 Spectral fitting

Spectral fitting is a crucial step following the computation of the frequency index in this analysis. While frequency index provides valuable insights into relative spectral amplitudes among different frequency bands, estimating the corner frequency through spectral fitting enhances the understanding of seismic source characteristics.

The method to determine earthquake source parameters through amplitude-spectral fitting was first introduced by James N. Brune, John Boatwright, and Raúl Madariaga. This technique analyses the frequency content of seismic waves to estimate details such as fault size, stress drop, and energy release. Subsequent refinements by researchers (Brune, 1970; Madariaga, 1976: Boatwright 1980). Brune's model (1970) effectively explains both near and far field spectra, facilitating the estimation of stress drop and source dimensions by comparing theoretical spectra with observed seismic data.

In Abercrombie's 1995 study, spectral modelling was applied to three-component P and S-waves using four variations of the Brune model to investigate the perceived scaling disparity between small and large earthquakes. This spectral method has since been widely used in research. For example, Köseoglu et al. (2013) applied it to determine source parameters in the Marmara Region, demonstrating its effectiveness for moderate and small-magnitude earthquakes. Stork et al. (2014) assessed the reliability of seismic moment and magnitude estimates derived from spectral analysis, comparing methods such as Brune, Boatwright, and time-domain approaches to identify the most accurate for microseismic events.

In this study, I employed the Brune model to estimate the corner frequency. The corner frequency represents the point where the high amplitude of low-frequency signals starts to decay as frequency rises. This parameter plays an important role in measuring the radiated energy from seismic sources. When a crack ruptures at a certain speed, it generates waves with a distinct spectral shape, featuring a low-frequency plateau and decay proportional to the square of the frequency. The corner frequency marks these two segments, and it's inversely related to the earthquake duration (Shearer, 2009).

The Brune model involves parameters such as n, γ, and t, reflecting Brune's original formulation for curve fitting. Here, $\Omega(f)$ represents seismic amplitude spectra, f_c is the corner frequency, and Q is the quality factor, all essential in characterizing seismic source characteristics. The model equation is:

$$\Omega(f) = \frac{\Omega_0 e^{-(\frac{\pi f t}{Q})}}{\left[1 + (\frac{f}{f_c})^{\gamma n}\right]^{1/\gamma}} \tag{2.2}$$

In this study, I employed the parameters $t = 0,\ \gamma = 1$ as proposed by Boatwright (1980), while n varied to optimize the model fit.

Before computing the corner frequency, spectral fitting involves converting the velocity spectrum to a displacement spectrum (Eyre et al., 2015; Shearer, 2009). This process focuses specifically on segments where the signal amplitude exceeds the noise level, as depicted in Figure 2.4.

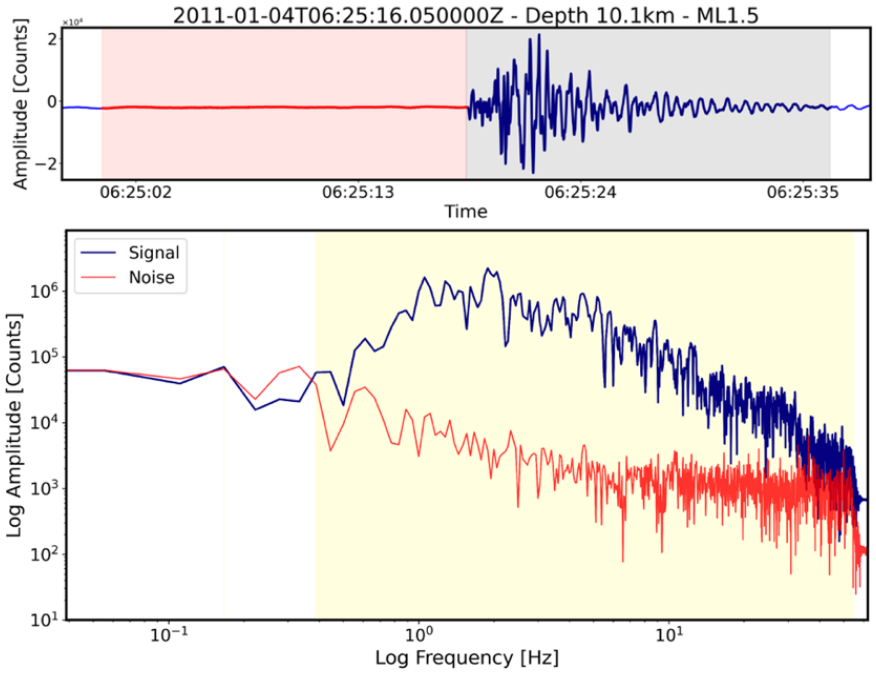

Figure 2.4 Comparison between signal and noise in the frequency domain for a single seismic waveform. The yellow area represents the selected frequency range for spectral fitting.

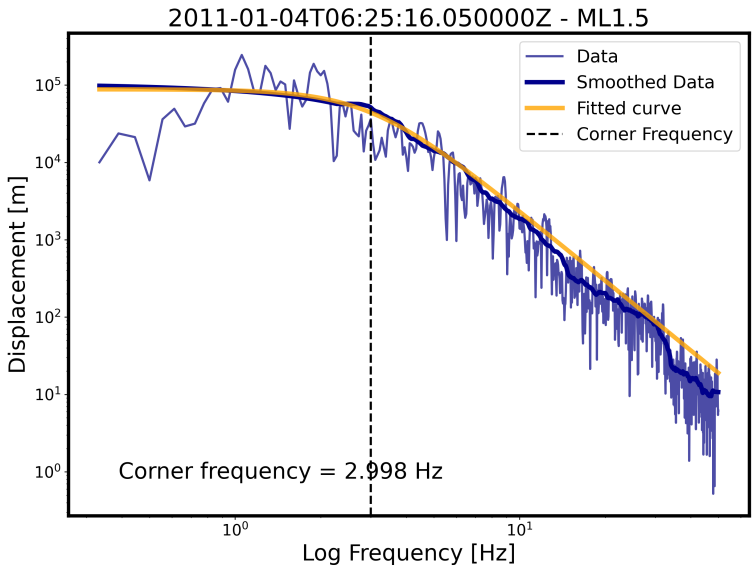

Figure 2.5 Example of spectra fitting for corner frequency estimation using Brune's model.

To determine the corner frequency, I first computed the seismic amplitude spectra. Subsequently, I applied a spectral smoothing technique before initiating the fitting process with the Brune model. The fitting process involved a grid search approach to find the optimal corner frequency (Greenfield et al., 2019). By iteratively fitting the model to the observed spectra with varying corner frequency values, the best-fitting parameters were determined. An example of the estimated corner frequency resulting from this process is illustrated in Figure 2.5.

2.4 Source radius

The radius of the seismic source is a critical parameter in understanding seismic phenomena. It represents the geometric extent of the fault or rupture zone associated with an earthquake. To calculate the stress drop from earthquake spectra, I typically assume a circular rupture geometry with radius r, which is often suitable for small magnitude earthquakes (Brune, 1970). Determining the corner frequency is essential because it informs the estimation of parameters such as the earthquake's stress drop and the radius of the fault or rupture. According to Brune (1970), the corner frequency is particularly significant as it helps establish the size and scale of the seismic source. The equation established by Brune (1970) is utilised to relate corner frequency to radius:

$$\mathrm{r} = \mathrm{k}\frac{\mathrm{V_p}}{\mathrm{f_c}} \tag{2.3}$$

Where k is a constant associated with the spherical average of corner frequencies for a particular theoretical model. One of the most referenced values is derived from Madariaga (1976), who conducted dynamic calculations using finite differences for a circular fault. Assuming a rupture velocity of 90% of the shear-wave velocity ($V_r = 0.9V_s$), Madariaga obtained k values of 0.32 and 0.21 for the p-wave and s-wave corner frequencies, respectively. In this study, parameter $\mathrm{k} = 0.32$ was used, for the p-wave analysis.

To calculate the P-wave velocity (V_p) in this study, I used the common relationship of $\mathrm{V_p} = \sqrt{3}\mathrm{V_s}$ (Baumbach & Bormann, 2011). The shear wave velocity ($\mathrm{V_s}$) was derived from the shear-wave velocity structure in the Larderello-Travale geothermal field, as detailed by Saccorotti (2014). It was determined that the average shear-wave velocity at a depth of 10 km is approximately 2.7 km/s.

2.5 Seismic moment

Seismic moment represents a measure of the size of an earthquake, depending on the area of rupture, the rigidity of the rock, and the amount of slip from faulting. It is calculated using the formula:

$$\mathrm{M_0} = \mu \mathrm{AD} \tag{2.4}$$

Where μ is a constant varying according to the material, A is the area of the ruptured fault, and D is the average slip (Rafferty, 2024). However, determining the seismic moment necessitates thorough examination of the source function. In this study, the equation proposed by Kanamori (1977) is employed for determining the seismic moment:

$$\mathrm{M_w} = \log_{10} \mathrm{M_0} + \mathrm{C} \tag{2.5}$$

Where $\mathrm{C} = -10.545$ (Kanamori (1977)). This equation establishes a direct link between the moment magnitude (M_w) and the seismic moment ($\mathrm{M_0}$), allowing me to quantify the earthquake's energy release.

Additionally, I converted the local magnitude ($\mathrm{M_L}$) to moment magnitude ($\mathrm{M_w}$) before calculating seismic moment ($\mathrm{M_0}$). By using the relationship for small earthquakes ($\mathrm{M_L} \lesssim 4.3$) as proposed by Malagnini and Munafò (2018) is employed:

$$M_w = \frac{2}{3} M_L + 1.14 \quad (2.6)$$

This relationship allows us to convert the local magnitude, which is often easier to measure and more commonly available in earthquake catalogues, to the moment magnitude, which is more directly related to the seismic moment.

Once moment magnitude M_w is determined, the seismic moment M_0 can be calculated using the following equation:

$$M_0 = 10^{(M_w - C)} \quad (2.7)$$

This methodology ensures that the seismic moments are accurately calculated from the available magnitude data, allowing for a reliable estimation of stress drops.

2.6 Stress drop

Stress drop is a key concept in seismology for understanding the mechanics of earthquakes and the behaviour of faults under tectonic stress. The stress drop is a measure of the difference in stress before and after an earthquake (Shearer, 2009). Normal earthquakes typically exhibit stress drop values ranging from 1 to 10 MPa (Kanamori and Anderson, 1975; Kanamori and Brodsky, 2004). However, long-period earthquakes, often found in volcanic or geothermal regions, tend to have lower stress drops. Studies by Greenfield et al. (2019) and Ide et al. (2007) have shown that these events frequently register stress drops below 1 MPa. These findings highlight the unique seismic characteristics and dynamics of long-period earthquakes. In this geothermal area focused study, the expectation of observing long-period earthquakes with stress drop values below 1 MPa is grounded in these characteristics, highlighting the distinct seismic behaviour influenced by fluid-related processes and slower slip velocities.

In this study, the fundamental principles outlined by Eshelby (1957) are used to estimate stress drops, particularly focusing on circular faults. By leveraging seismic moment (M_0) and the radius of the seismic source (r), a quantitative measure of stress drop is derived using the equation:

$$\Delta\sigma = \frac{16}{7}\frac{M_0}{r^3} \tag{2.8}$$

In principle, stress drop measures the permanent changes caused by an earthquake. However, estimating stress drops for small earthquakes involves analysing the waveform patterns of seismic body wave and making assumptions about the source dynamics. These estimates, often called Brune-type stress drops, are not direct measurements and rely on modelling assumptions that may not always hold true. Additionally, these measurements do not indicate the absolute stress level, which remains a controversial topic (Shearer, 2009).

In summary, the methodology presented here offers a comprehensive framework for analysing seismic activity in the Larderello-Travale geothermal field area. By leveraging earthquake catalog data, frequency index calculations, spectral fitting techniques, and estimations of parameters such as source radius, seismic moment, and stress drop. This study aims to gain insights into the region's seismological characteristics. The focus on long-period earthquakes highlights the need for specialised methodologies to understand their unique dynamics of the study area.

Chapter 3

Results

Here I present the frequency index data (section 3.1), corner frequency (section 3.2) and stress drop estimates (section 3.3) of the 1,577 earthquakes in the Lardarello-Travale geothermal field recorded by the TRIF seismic station from January 2011 to April 2024 (Fig. 3.1).

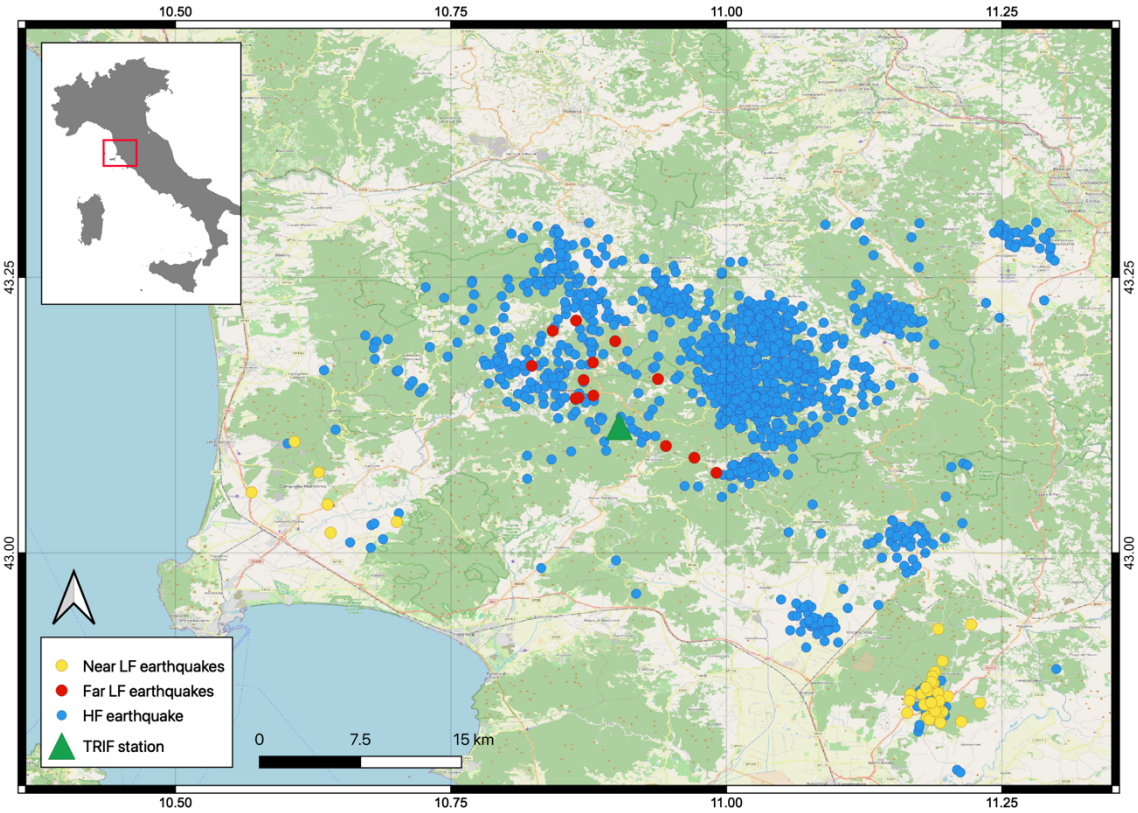

Figure 3.1. Map of the 1,577 earthquakes recorded by the TRIF seismic station (green triangle) in the period January 2011 to April 2024 in the Larderello-Travale geothermal field area and nearby. The normal-type, high-frequency earthquakes are marked in blue, the long-period earthquakes within 15 km of the TRIF station in red and those beyond 15 km in yellow.

3.1 Frequency Index (FI)

As outlined in the methodology section, the frequency index (FI) allows to distinguish between low-frequency and high-frequency earthquakes by analysing the spectral amplitudes across different frequency bands of earthquakes yields an understanding of the energy distribution of the seismic signals.

To interpret the FI values, I focused on earthquake events with high FI values and compared their waveforms with those of events with low FI values. Through careful visual inspection of the waveforms, the aim was to identify distinct characteristics associated with low-frequency seismic events.

It was observed that earthquake events with FI values above 1.25 (Figures 3.2) exhibited waveform features indicative of low-frequency seismic waveforms or long-period earthquake. They show longer durations amplitudes and last longer, compared to events with FI values below 1.25 (Figures 3.3). This analysis allowed us to establish a threshold of FI = 1.25 as a criterion for distinguishing between low-frequency and high-frequency events. Figures 2.2 and 2.3 in chapter 2 show examples of FI calculations for long period and regular events.

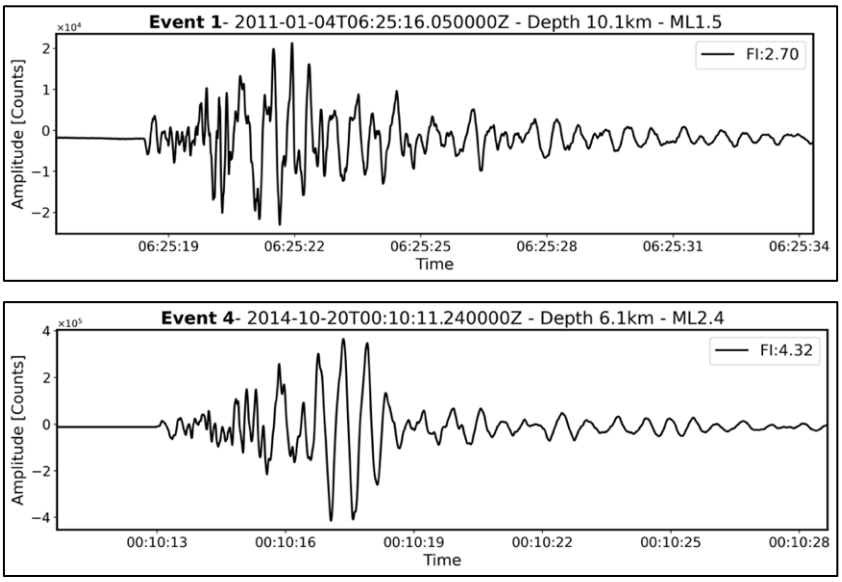

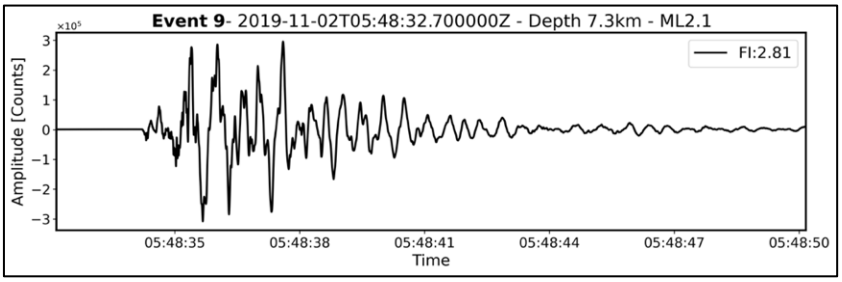

Figure 3.2. Example of waveforms of earthquakes with FI values larger than 1.25 with time window of 2 seconds before and 18 seconds after p-wave arrival.

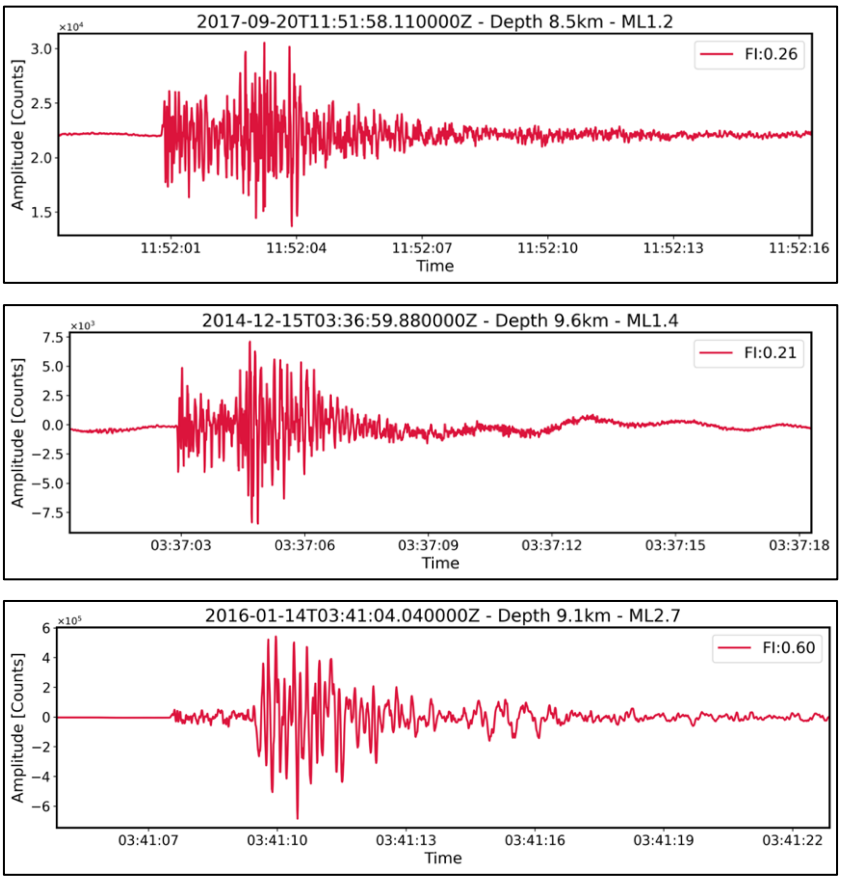

Figure 3.3. Example of waveforms of earthquakes with FI values smaller than 1.25 with time window of 2 seconds before and 18 seconds after p-wave arrival.

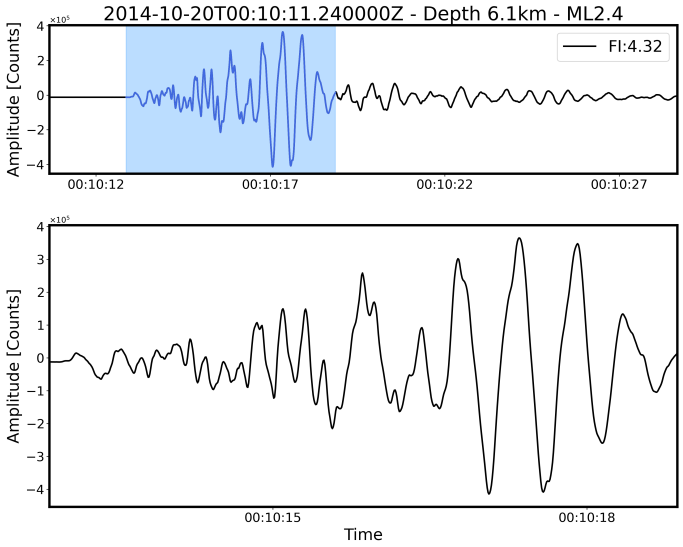

Figure 3.4. Example of low-frequency waveform for an earthquake with an 18-second time window (top) and a zoomed-in 6-second time window (bottom).

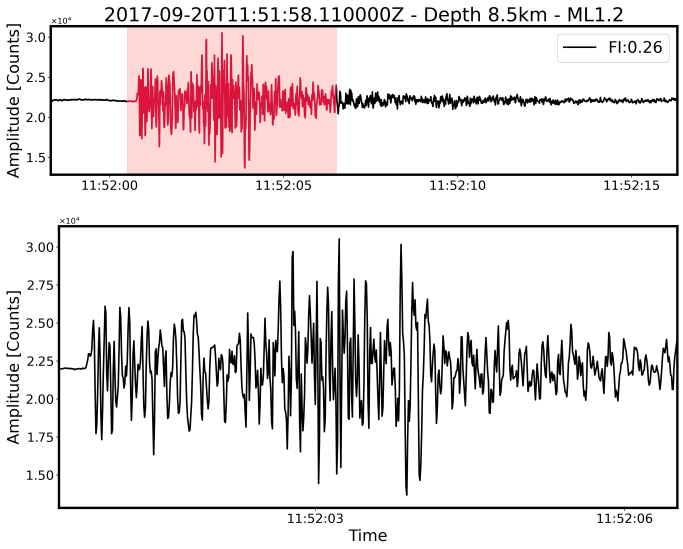

Figure 3.5. Example of high-frequency waveform with 18 seconds time window (top) and zoomed in waveform for 6 seconds time window (bottom).

Figure 3.4 provides an example of long-period earthquakes with an 18-second time window (top) and a zoomed-in 6-second time window (bottom). This figure highlights the longer duration of the event compared to high-frequency (i.e., normal-type) earthquakes. Figure 3.5 presents an example of a high-frequency

waveform of an earthquake with an 18-second time window (top) and a zoomed-in 6-second time window (bottom). This figure shows the shorter duration characteristic of high-frequency events. These observations support the use of FI as a quantitative measure to identify earthquakes with low-frequency content, often associated with specific geological processes or fault mechanisms in the study area.

Out of the 1,577 seismic events detected by the TRIF station, only 51 events exhibited high frequency index (FI) values, larger than 1.25 (i.e., long-period earthquakes). However, in selecting events for closer examination, the focus was on those within a 15 km radius of the TRIF station (Figure 3.1).

The rationale behind this selection criteria was to ensure proximity to the station for more accurate waveform characterization and to mitigate potential issues related to attenuation and signal quality for events farther away. Upon closer inspection, the waveforms of events beyond this range did not exhibit clear characteristics and showed a low signal-to-noise ratio. As Buurman & West (2010) suggest, there are limitations when using dominant frequency to represent the overall frequency content. Earthquakes with low signal-to-noise ratios are prone to low-frequency noise contamination, especially with broadband data, suggesting possible attenuation effects (see Figure 3.6 and 3.7 for example).

The authenticity of 13 selected long-period earthquakes was verified to distinguish them from seismic events that might appear low-frequency due to propagation effects. This verification is crucial, as it confirms that both long-period and regular earthquakes occur in the same location, highlighting the significance of our findings. Long-period events, often referred to as slow earthquakes, exhibit distinct source characteristics that differentiate them from high-frequency events.

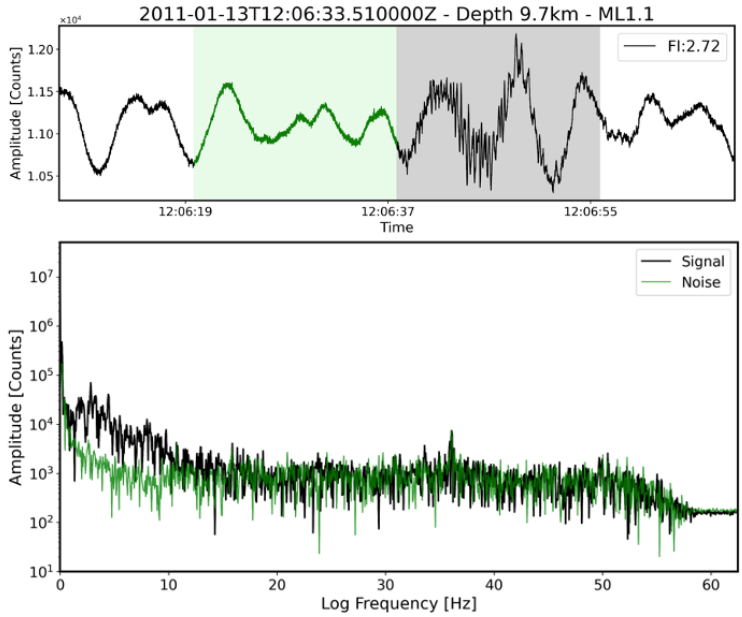

Figure 3.6. Example of seismic signals with a high FI (> 1.25) that show low signal to noise ratio.

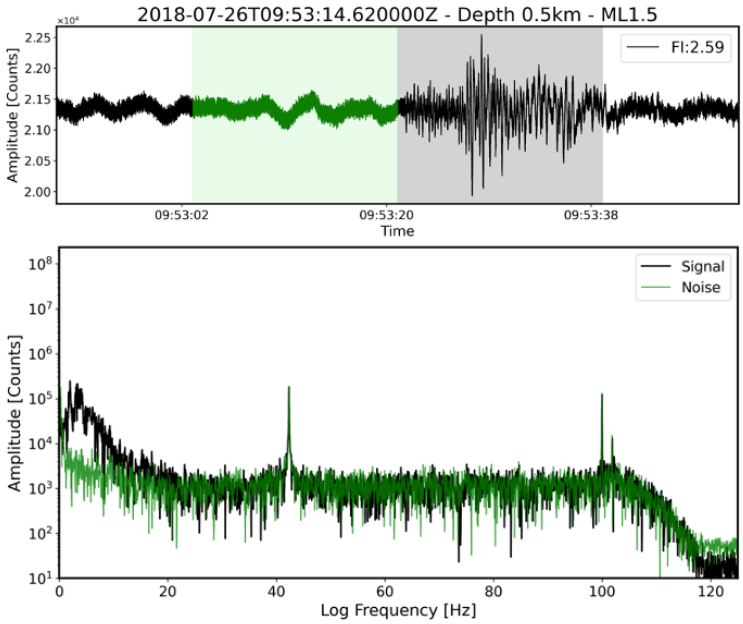

Figure 3.7. Example of two seismic signals with a high FI (> 1.25) that show low signal to noise ratio.

Figure 3.8 illustrates the two locations where both types of earthquakes have occurred, demonstrating that the detected long-period events in our study are intrinsic to their source mechanisms and not artifacts of propagation effects. This figure highlights that different kinds of earthquakes can occur in the same location, emphasizing the variety of seismic activity in the area. Figure 3.9 provides a comparison of nearby earthquake waveforms. In panel (a), long-period earthquakes (event 3) are shown in blue and normal earthquakes in red, occurring 0.57 km apart. In panel (b), long-period earthquakes (event 9) are shown in blue and normal earthquakes in red, occurring 0.9 km apart.

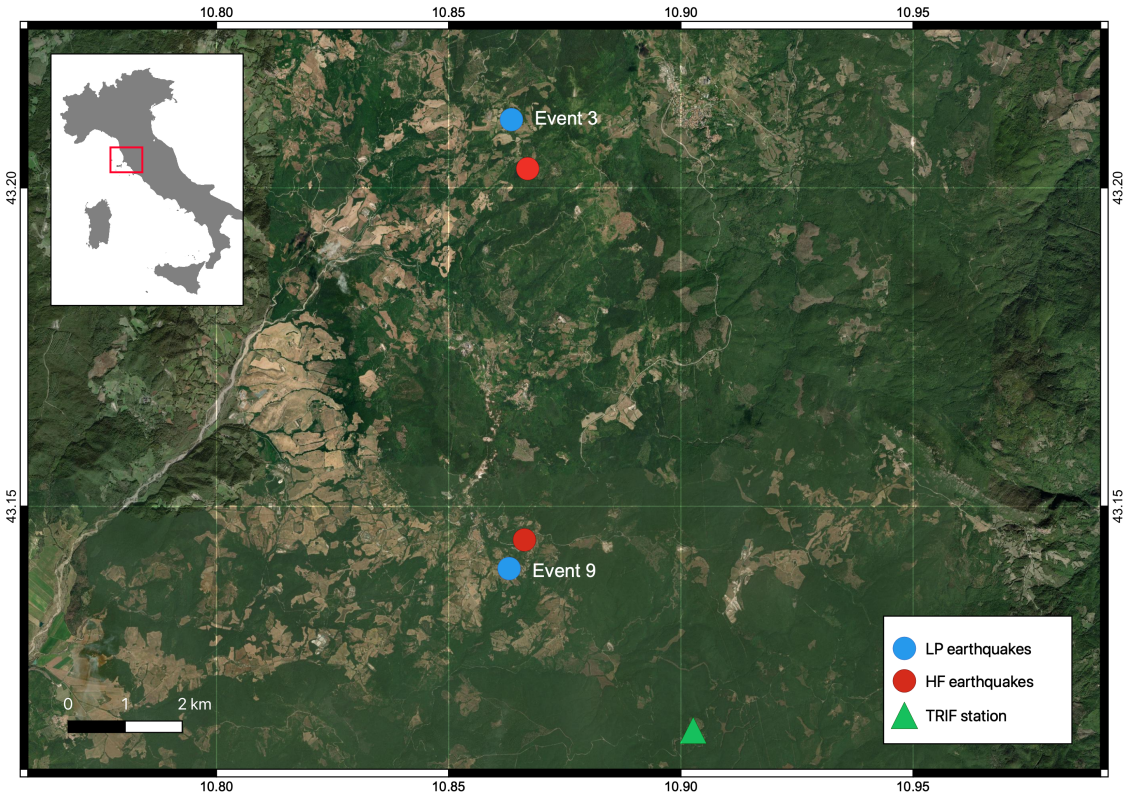

Figure 3.8. Map indicates the locations of the long-period earthquakes (event 3 and event 9) and regular earthquakes.

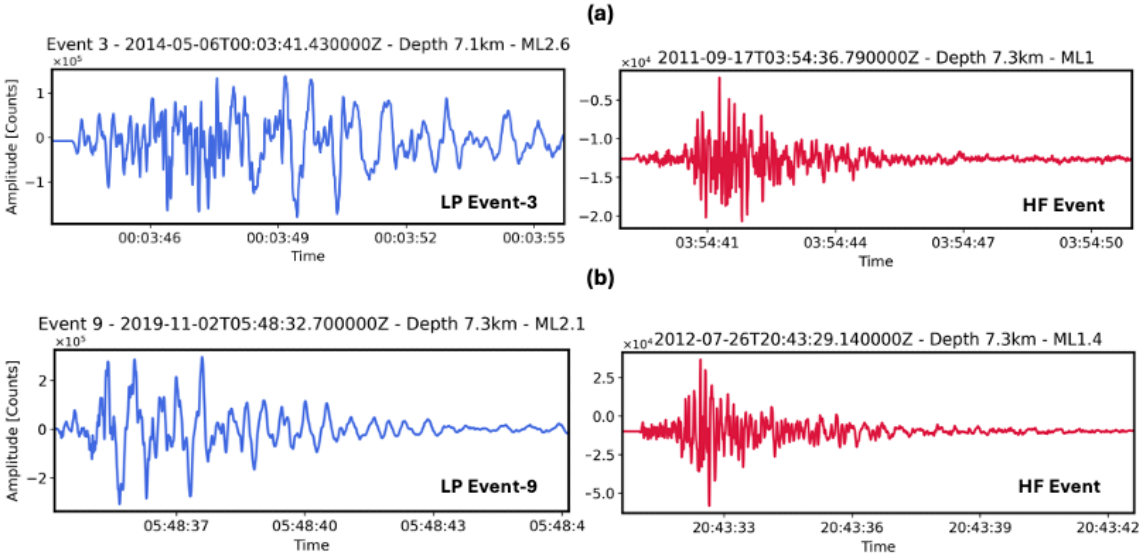

Figure 3.9. Comparison of nearby earthquake waveforms. (a) Long-period earthquakes (event 3) in blue and normal earthquake in red (0.57 km Apart). (b) Long-period earthquakes (event 9) in blue and normal earthquake in red (0.9 km Apart).

The decision to focus on events near the TRIF station allows for a more detailed study of their waveform features and provides greater confidence in the results. However, it is essential to acknowledge the potential limitations associated with this approach and the need for further investigation into events beyond the 15 km radius to fully understand their seismic characteristics.

Figure 3.10 presents a histogram that categorizes 1,577 earthquakes based on their FI values. It distinguishes between long-period events (FI > 1.25) and regular events (FI < 1.25), providing a comprehensive view of the frequency characteristics within the dataset. In Figure 3.11, FI values are plotted against the distance from the TRIF station. This plot highlights 13 selected events in blue, demonstrating how FI values vary with distance.

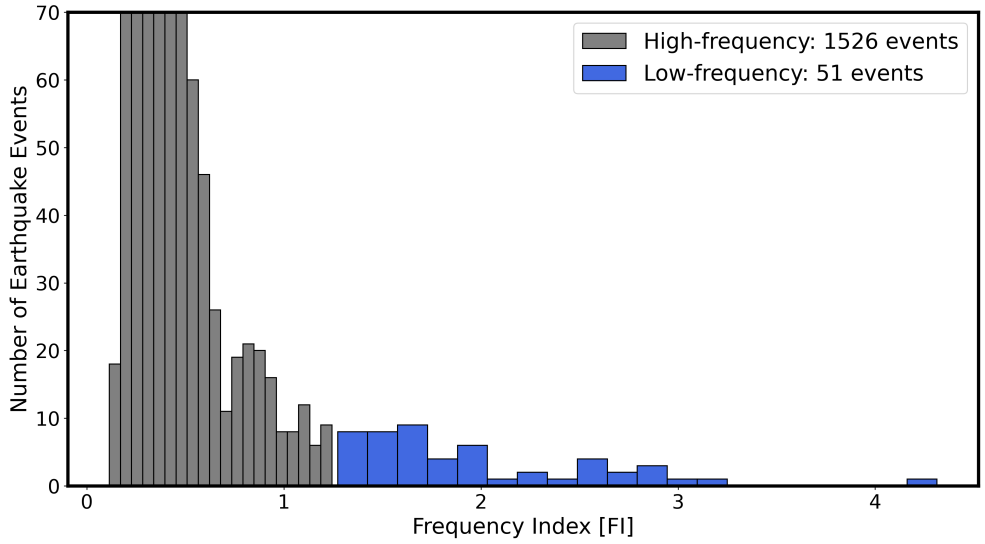

Figure 3.10. Histogram of FI values for 1577 earthquakes, distinguished between Low-Frequency (FI> 1.25) and High-Frequency (FI<1.25) events.

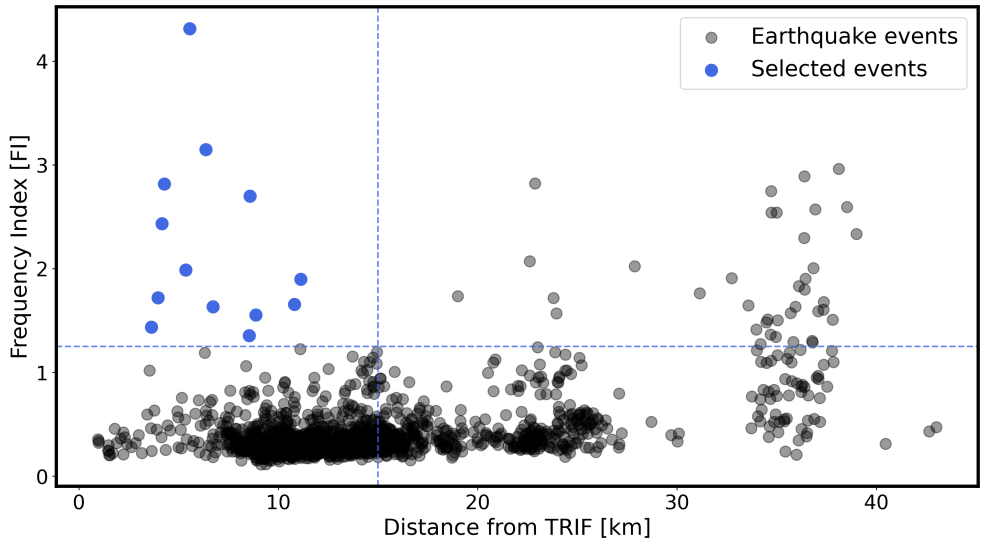

Figure 3.11. Frequency Index (FI) versus Distance from TRIF station. The 13 selected events are in blue colour.

Thirteen low-frequency events were selected for this study (Table 3.1 and Figures 3.1). These events, play a crucial role in our analysis of seismic activity within the Larderello-Travale geothermal field.

Event	Origin Time	Latitude	Longitude	Depth (km)	FI	f_c	M_0	r	$\Delta\sigma$
1	2011-01-04 06:25:16.050	43.192	10.899	10.1	2.7	4.403	4,841,723,675,841	498.572	0.017
2	2011-06-10 23:42:13.580	43.097	10.945	8.9	1.72	3.837	4,152,726,538,879	513.12	0.013
3	2014-05-06 00:03:41.430	43.2107	10.8635	7.1	1.9	2.694	26,201,933,093,237	589.633	0.056
4	2014-10-20 00:10:11.240	43.1577	10.9378	6.1	4.31	4.128	19,275,249,131,909	457.801	0.088
5	2023-07-13 03:27:45.980	43.1427	10.8792	7.6	1.35	3.237	4,152,726,538,879	461.761	0.018
6	2016-11-04 14:06:20.830	43.0863	10.9708	4.4	3.15	4.775	4,152,726,538,879	455.152	0.019
7	2019-08-13 12:26:09.210	43.2015	10.8423	2.6	1.66	3.087	30,549,211,132,155	531.173	0.089
8	2019-11-02 04:28:58.460	43.1408	10.8657	5.8	2.43	4.512	12,161,860,006,464	443.274	0.061
9	2019-11-02 04:29:14.780	43.1568	10.8703	6	1.99	4.48	12,161,860,006,464	427.919	0.068
10	2019-11-02 05:48:32.700	43.1402	10.863	7.3	2.82	4.28	12,161,860,006,464	470.778	0.051
11	2020-12-15 03:20:21.360	43.1727	10.8788	6.2	1.63	5.093	3,054,921,113,216	414.854	0.019
12	2023-02-02 01:47:36.870	43.1697	10.8233	8.9	1.55	1.453	2,620,193,309,324	457.661	0.012
13	2023-07-13 03:27:45.980	43.1427	10.8792	7.6	1.44	4.565	2,620,193,309,324	327.43	0.033

Table 3.1. Selected long-period earthquake events (or with FI > 1.25) in the Lardarello-Travale area recorded by the TRIF station in the period January 2011 to April 2024 (see also Figure 3.1).

3.2 Corner frequency and Spectral fitting

Corner frequency (f_c) is the point where the high-frequency spectral decay transitions to low-frequency spectral level (Figure 2.5). The corner frequency is a critical parameter for understanding the rupture process and the stress drop associated with these events. For the identified 13 low-frequency earthquake events.

For each earthquake, the observed spectral data was fitted to Brune's model using a grid search approach to optimize f_c (Greenfield et al., 2019) (see

Methods section 2.3). The parameters n and γ in the Brune's function (see equation 2.2) are adjusted to achieve the best fit. Our analysis was focused on areas where the signal exceeded the noise in the amplitude spectrum, ensuring accuracy in our estimations. Moreover, to enhance our understanding of seismic event dynamics, integrated spectrum analysis was conducted, converting seismic data into displacement amplitude. In this study, the estimated corner frequencies for the 13 long-period events are presented (see Figure 3.12 and 3.13).

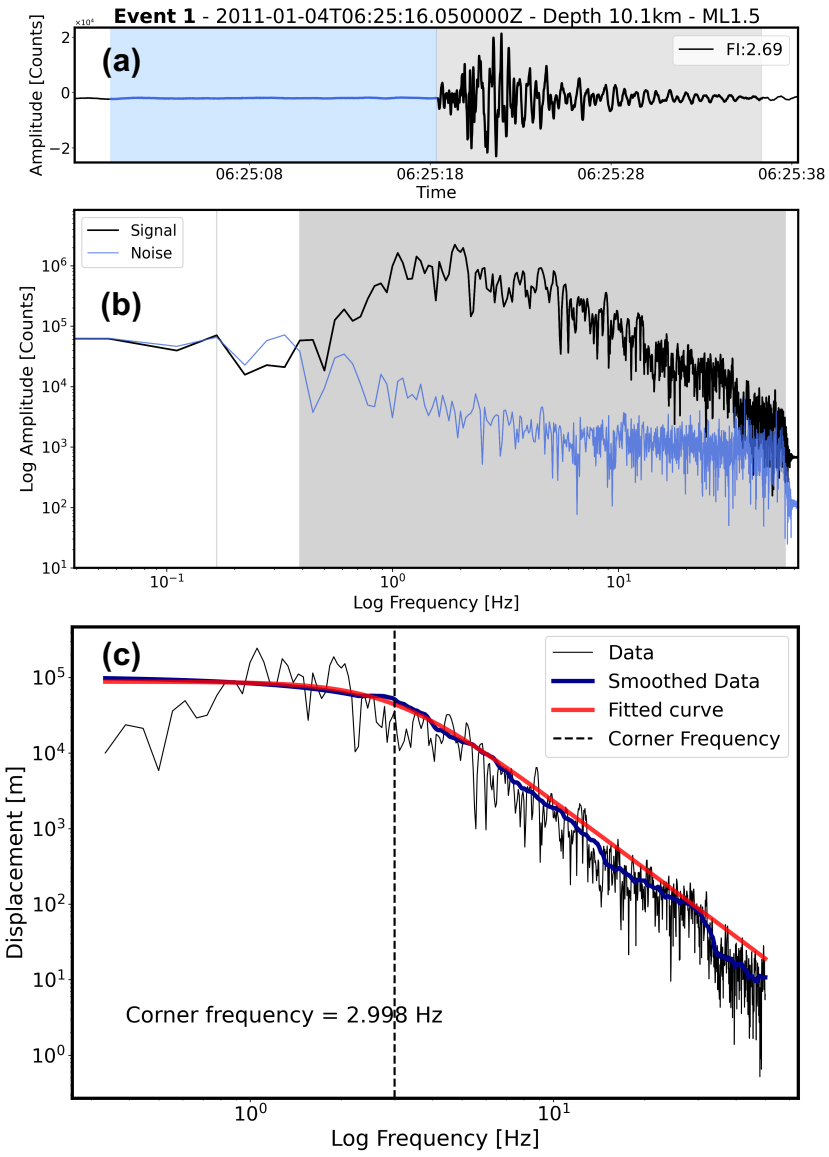

Figure 3.12. Example of spectral fitting for long-period earthquake event 1. (a) represent the waveform that highlight noise and signal area in blue and grey

respectively. (b) is a comparison of amplitude spectral of signal and noise, highlighted in grey is the area with higher signal than noise. (c) represent curve fitting of the signal.

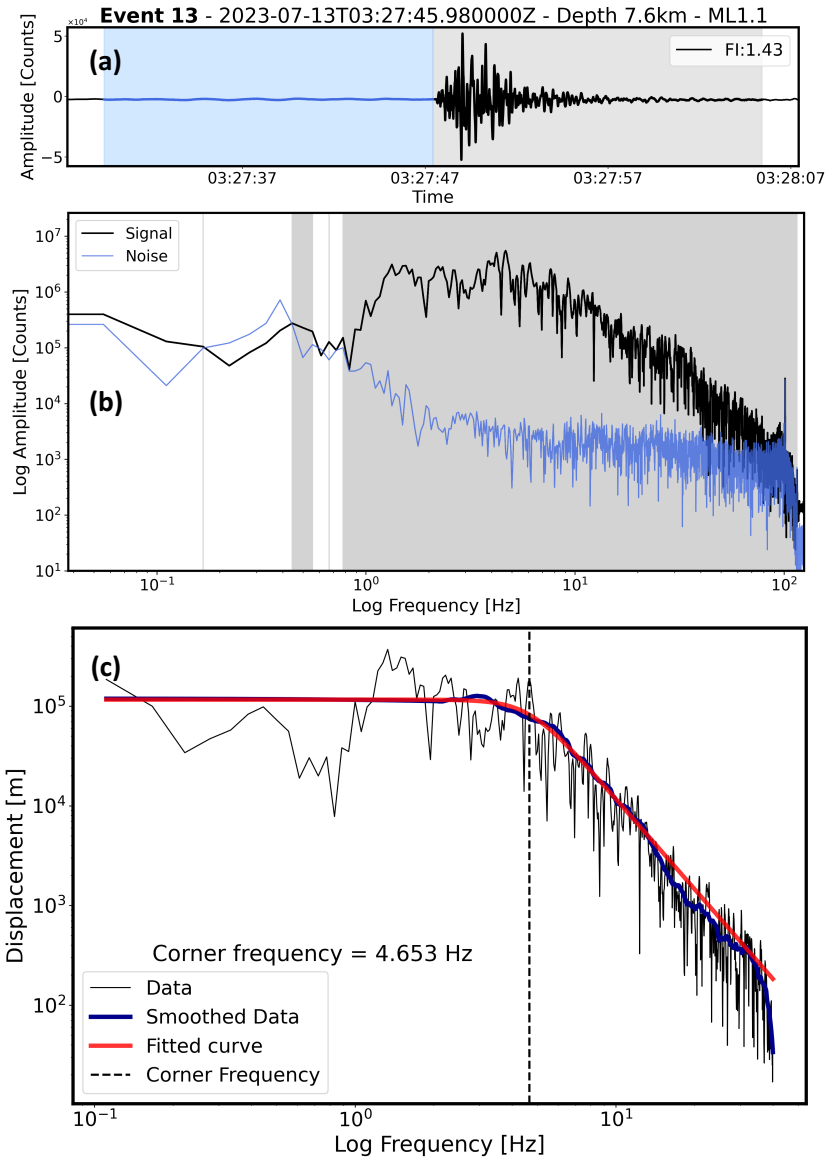

Figure 3.13. Example of spectral fitting for a long-period earthquake event 13. (a) represents the waveform that highlights the noise and signal area in blue and grey respectively. (b) is a comparison of amplitude spectral of signal and noise, highlighted in grey is the area with higher signal than noise. (c) represents the curve fitting of the signal.

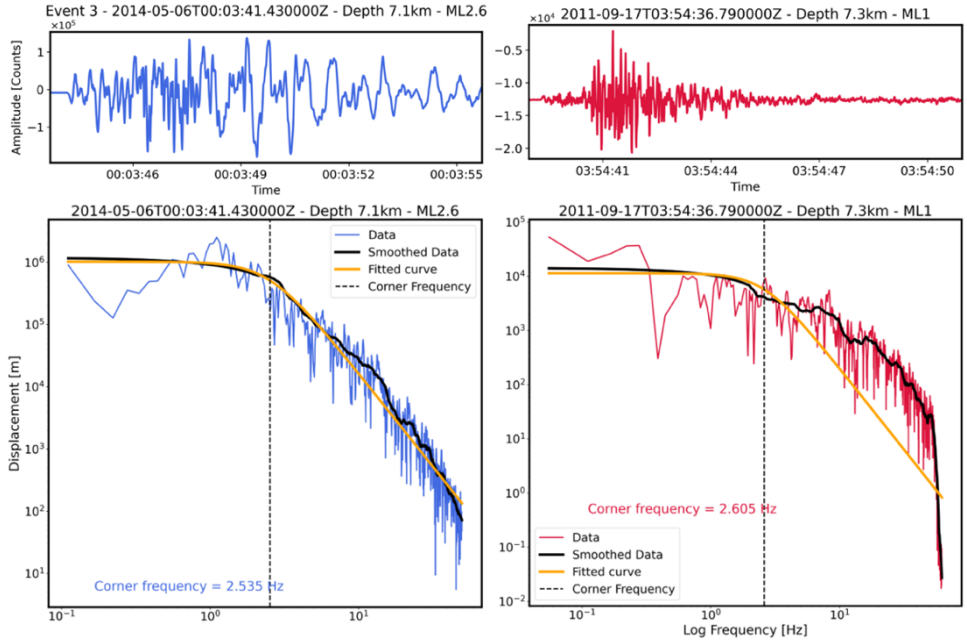

Figure 3.14. Comparison of nearby earthquake events. (left) Long-period earthquakes (event 3). (right) high-frequency or normal earthquake.

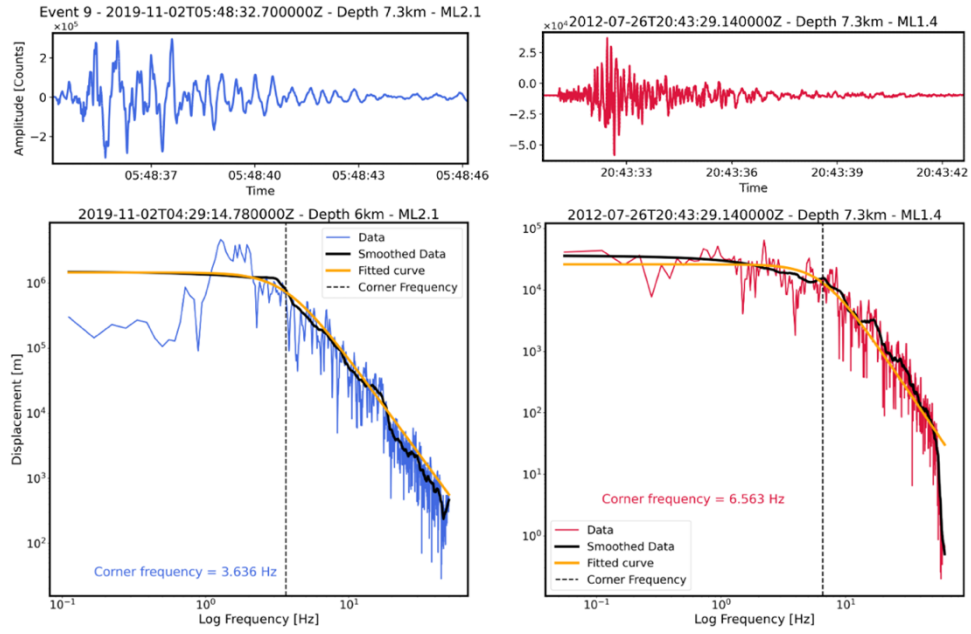

Figure 3.15. Comparison of nearby earthquake events. (left) Long-period earthquakes (event 9). (right) high-frequency or normal earthquake.

Moreover, to validate my finding that the selected events do not exhibit long-period characteristics solely due to propagation effects, I conducted a spectral fitting to estimate corner frequencies for different types of earthquakes occurring at the same location. Refer to Figure 3.14 and 3.15 for details.

Based on the findings from section 3.1 and corner frequency estimation in the current section (3.2), they show that the displacement spectral amplitude of the two different earthquakes occurred at the same location are different, with different values of corner frequency. I can confirm that the long-period earthquakes identified are not solely attributable to propagation effects. This conclusion is supported by studies (Clarke et al., 2021), which suggest that seismic events of different types occurring in close proximity are influenced by fluid migration and resonance within volcanic conduits and fractures.

3.3 Stress drop

The stress drop is a measure of the difference in stress before and after an earthquake, which provides insights into the energy released during the rupture process. This parameter is critical for understanding the mechanics of earthquake generation and the conditions within the subsurface in the Larderello-Travale geothermal field. The stress drop for each of the 13 long-period earthquakes was estimated starting from fc, M_L , M_W and M_0 (see Methods section 2.6).

Figures 3.16 and 3.17 display the distribution for the 13 long-period earthquake events in the study area of stress drop ($\Delta\sigma$) versus seismic moment (M_0) and moment magnitude (M_w), respectively. These plots reveal that all selected long-period events have stress drop values below 1 MPa. The grey background region represents the global range of stress drop estimates (1–100 MPa) (Kanamori and Brodsky, 2004) for normal-type earthquakes (or high-frequency), highlighting how the stress drop values of these long-period events compare to global seismic data.

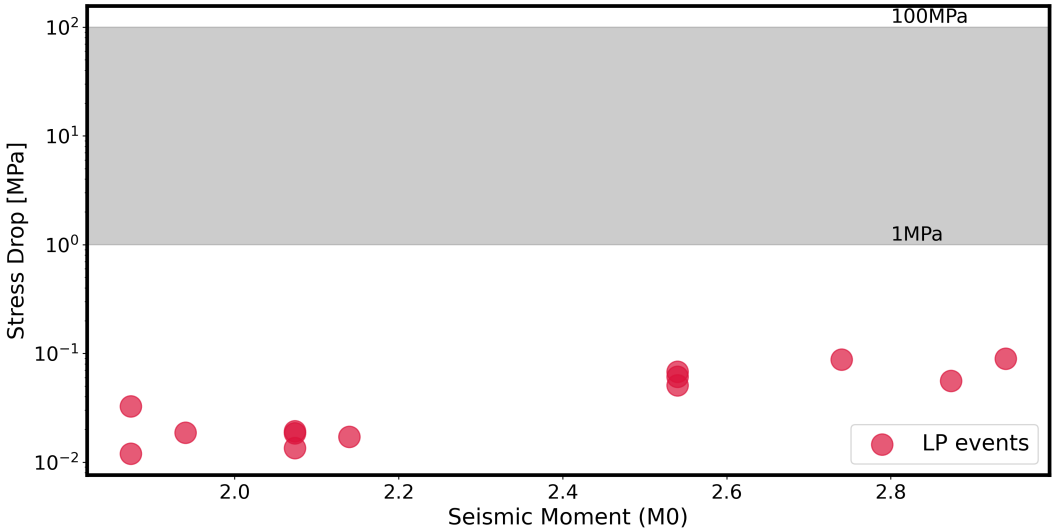

Figure 3.16. Relationship between stress drop ($\Delta\sigma$) and moment magnitude (M_w).

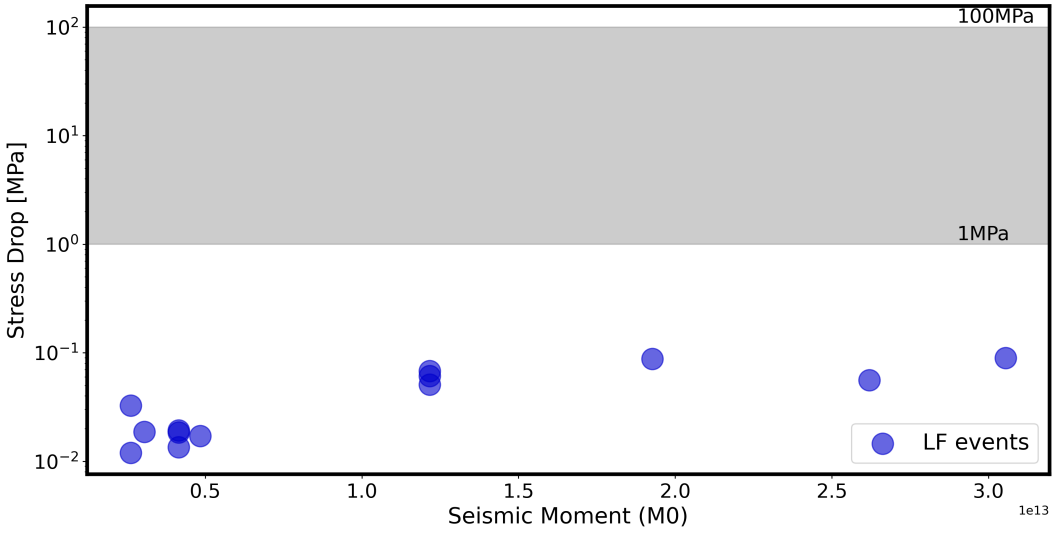

Figure 3.17. Relationship between stress drop ($\Delta\sigma$) and seismic moment (M_0).

Chapter 4

Discussion

4.1 Overview

This study represents the first identification and characterization of long-period earthquakes within the Larderello-Travale geothermal field. These unique seismic events have never been documented before in this particular geothermal area or anywhere else in Italy, offering an interesting contribution to seismic research.

The primary objective is to distinguish low-frequency or long-period earthquakes using frequency index (FI) analysis. Once these long-period earthquakes are identified, the analysis focuses on determining their stress drop. This process involves a detailed estimation of their corner frequencies through spectral fitting and subsequently calculating the stress drop for selected events.

The key findings include:

- Identification of long-period earthquake events: A threshold frequency index value of 1.25 was established to differentiate between low-frequency and high-frequency seismic events and a set of long-period earthquakes is identified. Out of the 1577 seismic events detected by TRIF station from 2011 to 2024, 13 events within a 15 km radius of the TRIF station were identified as low frequency (Figure 3.1 and Table 3.1).
- Analysis of corner frequencies and spectral fitting: I estimated corner frequencies for the 13 identified long-period events to determine the stress drops associated with each event (Figure 3.1 and Table 3.1).

- Stress drop estimation: The stress drop values for the 13 long-period earthquakes ranged from 0.012 MPa to 0.089 MPa (Table 3.1), significantly lower than the stress drop global range (1-30 MPa) for normal earthquakes (Kanamori and Brodsky, 2004).

4.2 Identification of long-period earthquakes

In this study, 13 out of 1,577 seismic events were identified as long-period (or low-frequency) seismic events using a frequency index (FI) threshold of 1.25 (Figure 2.2 and 2.3). To the best of my knowledge, this marks the first detection of these distinctive earthquakes ever recorded in Italy. This groundbreaking discovery will enable exploration into the migration of fluids at depth, fault slip dynamics, and other phenomena crucial to understanding geothermal contexts. For instance, research conducted at the Hengill geothermal volcanic complex in Iceland (Jousset et al., 2010) suggests that the operation of geothermal systems may induce long-period earthquakes due to pressure changes near wells caused by fluctuations in geothermal fluid extraction rates. Additionally, studies by Ide et al. (2007) demonstrate that low-frequency events are often associated with slow slip events occurring in deeper fault zones, where physical conditions such as increased pressure and temperature promote slower rupture processes.

The TRIF station, located at the heart of the Larderello-Travale geothermal field, was selected as the primary data source for this study (Figure 4.1). The decision to focus on seismic events within a 15 km radius of the TRIF station results from various factors (refer to section 3.1 and 3.2). This choice ensures a higher signal-to-noise ratio and better data quality for events detected by the station, optimising the accuracy of waveform characterization. By prioritising events in closer proximity, the effects of attenuation are reduced, ensuring more reliable seismic data for interpretation. However, it is important to acknowledge the potential limitations of this approach. Long-period earthquake events occurring beyond this range may be subject to increased attenuation, leading to signal degradation and reduced accuracy in waveform characterization. While 13

Long-period events within the 15 km radius are given priority, further study of the events beyond this range is necessary.

4.3 Long-period earthquakes in relation to geothermal features

4.3.1 Spatial analysis

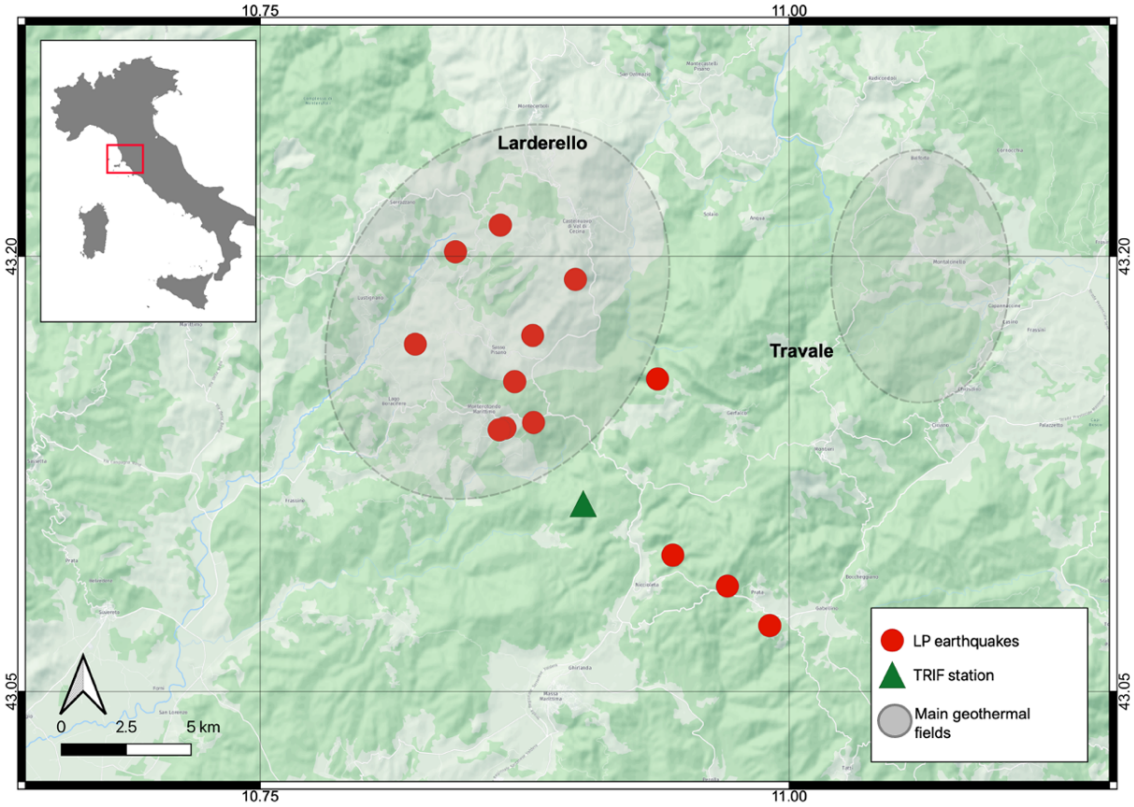

Figure 4.1. Map illustrating the TRIF station (green triangle), long-period earthquakes (red circles), and main geothermal fields (shaded areas) (modified from Batini et al., 2003 and Enel Green Power).

Spatial analysis was conducted to examine the distribution of the long-period events within the Larderello-Travale geothermal field and its vicinity. Figure 4.1 provides a map illustrating the locations of identified earthquakes

overlaid near key geothermal features and infrastructure. The spatial distribution reveals some low-frequency seismic events around geothermal areas.

A sketch map of the Larderello-Travale area (Figure 4.1), modified to highlight the main geothermal area from Batini et al., 2003, provides context for understanding the spatial distribution of seismic events. Key features such as the main geothermal fields, the TRIF station, and the locations of long-period earthquakes are delineated. As illustrated in Figure 4.1, most long-period events are clustered within the boundaries and vicinity of the geothermal field.

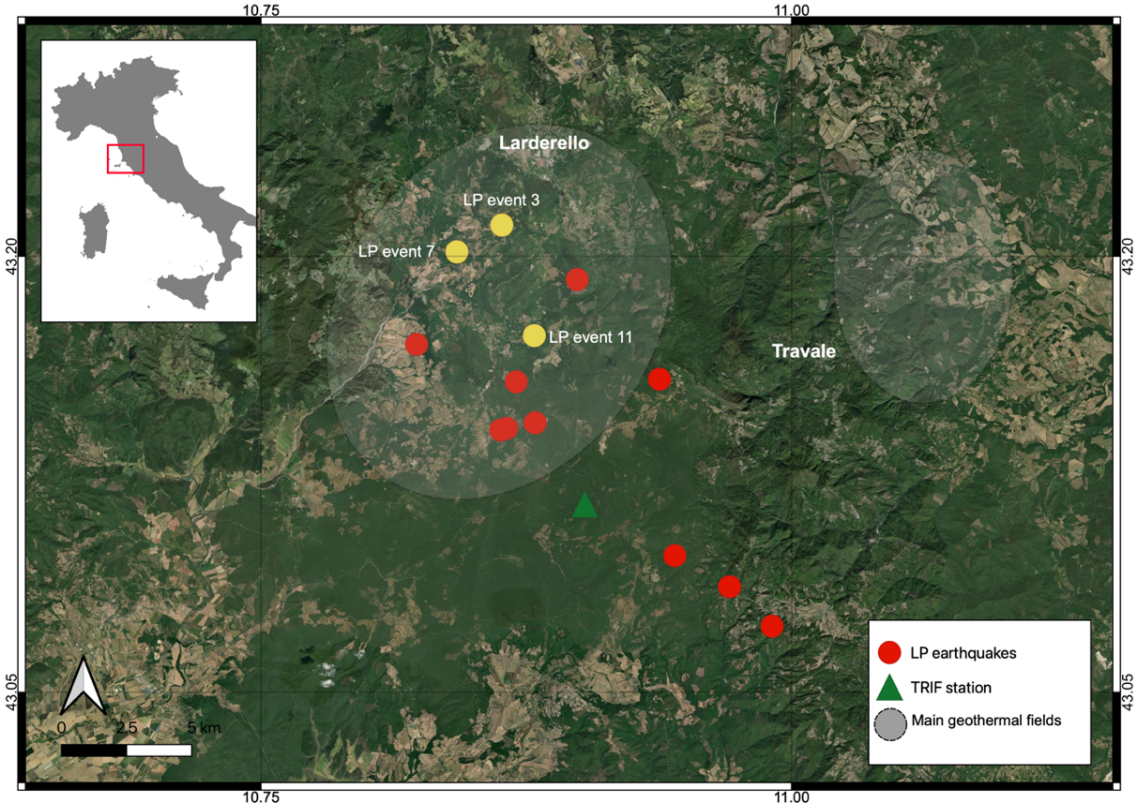

Figure 4.2. Long-period earthquakes occur in close proximity to geothermal infrastructures within the Larderello-Travale area.

Figure 4.2 shows that long-period earthquakes occur in close proximity to geothermal infrastructures within the main geothermal area of the Larderello field.

Figures 4.3, 4.4, and 4.5 reveal the close look of some long-period earthquakes occur in close proximity to geothermal infrastructures within the Larderello-Travale area, at distances ranging from approximately 300 to 960 meters. These earthquakes are possibly associated with anthropogenic activities related to geothermal operations (Jousset et al., 2010).

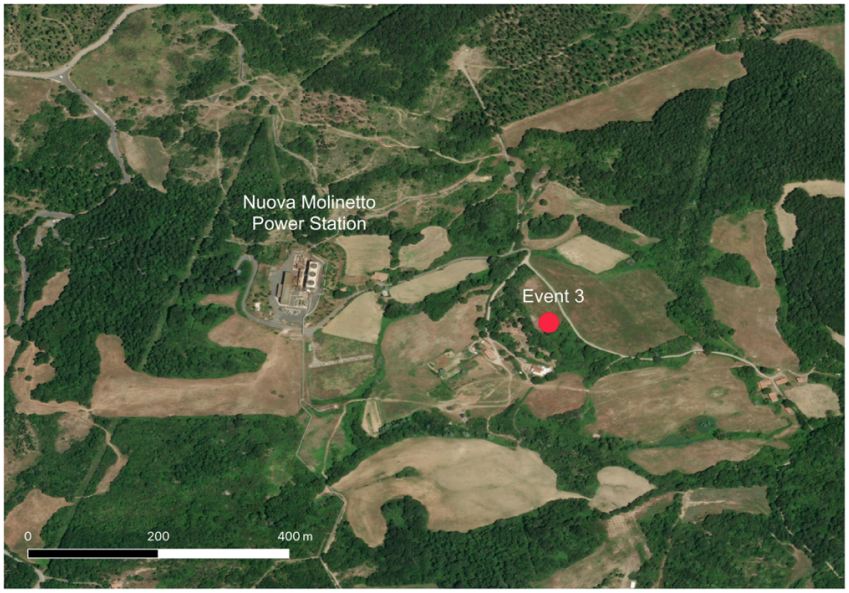

Figure 4.2. Map of the location of long-period earthquake (event 3) and the nearby Geothermal Infrastructure (Nuova Molinetto power station), approximately 300 metres apart.

Figure 4.3. Map of the location of long-period earthquake (event 7) and the nearby Geothermal Infrastructure (Le Prata power station), approximately 950 metres apart.

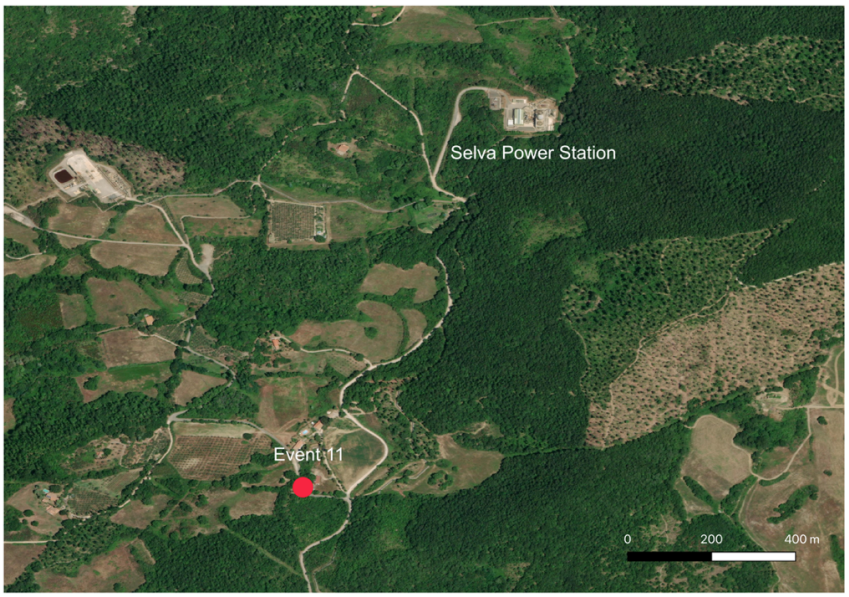

Figure 4.4. Map of the location of long-period earthquake (event 11) and the nearby Geothermal Infrastructure (Selva power station), approximately 300 metres apart.

Additionally, Figure 1.1 in Chapter 1 presents a geological sketch map of the Larderello geothermal area (adapted from Bertini et al., 2006, with geological features from Lazzarotto et al., 2002a, b). This map includes main fault lines and rock formations, providing a comprehensive view of the geological framework influencing the long-period earthquakes identified in this study. The spatial correlation illustrated in Figure 1.1 indicates that some long-period earthquakes align with the main fault lines, suggesting a potential link between these seismic activities and the faults.

4.3.2 Depth distribution analysis

The analysis of depth distribution among long-period earthquakes within the geothermal field demonstrates the relationship between earthquake depth and moment magnitude (M_w) for 13 identified long-period events (Figure. 4.6). This plot consistently shows that all detected long-period earthquakes occurred at depths shallower than 10 km.

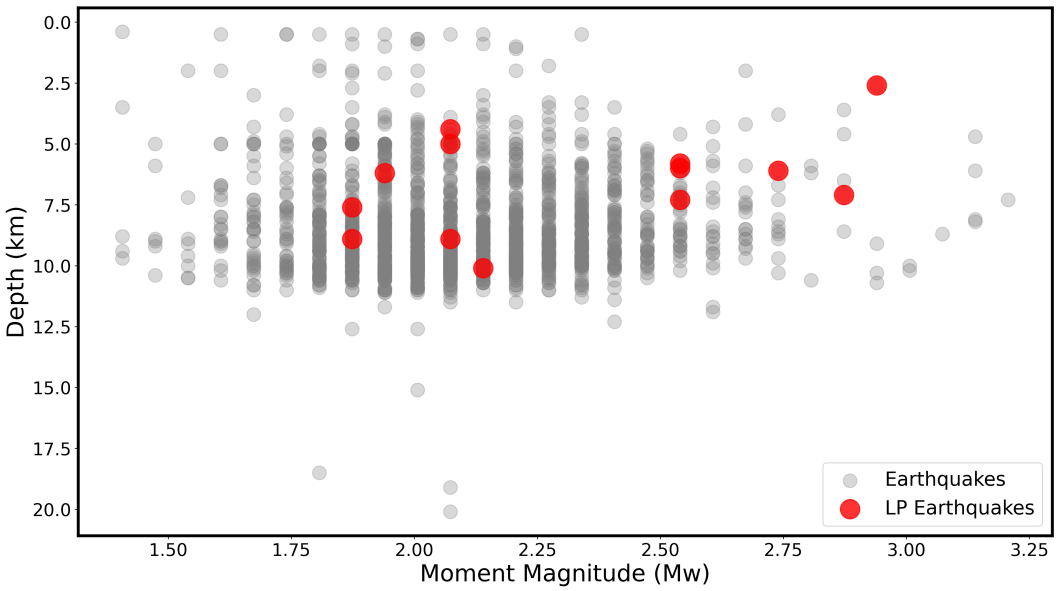

Figure 4.6. Depth vs Moment Magnitude (M_w) of 13 selected long-period earthquakes.

In the Larderello-Travale geothermal fields, geothermal well depths typically range from approximately 1000 to 4000 metres (Arias et al., 2010). Arias et al. (2010) document a total of 13 deep wells and numerous shallow wells in the Larderello-Travale system. These shallow depths align closely with where the selected long-period earthquakes have been observed, primarily within the shallow crustal layers (less than 10 km deep). This may suggest a potential relation between the geological processes generating long-period earthquakes and the distribution of geothermal wells.

4.3.3 Temporal relationship analysis

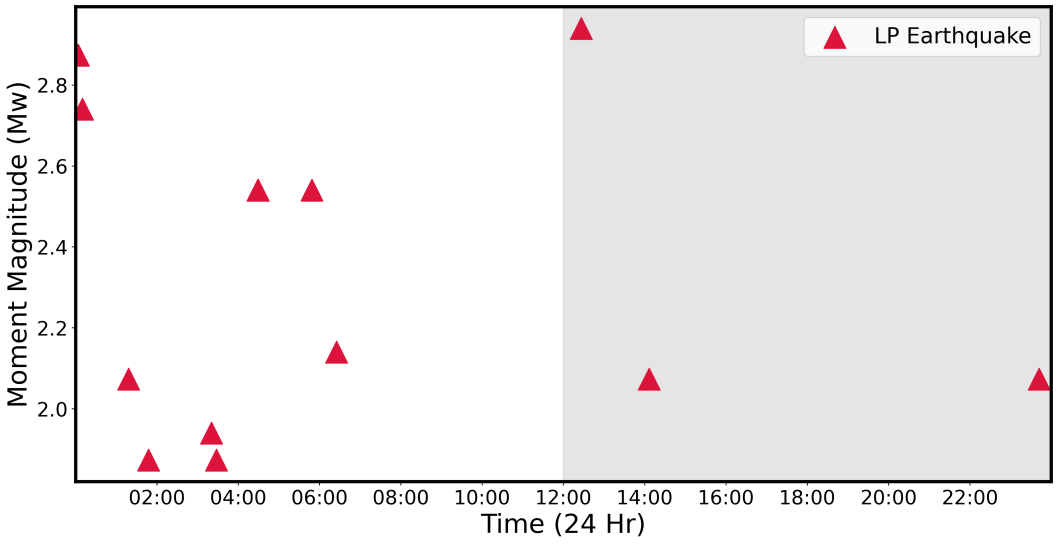

Figure 4.7 Timeline of long-period seismic events on a 24-hour scale.

A temporal relationship analysis indicates that long-period earthquakes occurred randomly throughout the day and night (Figure 4.7). These findings suggest that the trigger time of seismic events may not be influenced by scheduled geothermal operations, or other anthropogenic activities at the geothermal fields, which typically occur during daytime hours. This temporal randomness implies that these events are likely driven by internal physical processes within the geothermal field, such as fluid movements (e.g., Fujita & Ida, 2003). However, it is crucial to note that while these events do not show a

clear preference for occurring during daytime hours, suggesting they are less likely triggered solely by anthropogenic activities, the possibility remains that geothermal operations could still play a role in their triggering.

4.3.4 Resonating of coda wave

In this study, resonance patterns were observed in the coda of certain long-period earthquakes (Figure 4.8). The waveform analysis reveals a distinct low-frequency signal followed by a prolonged coda wave. This phenomenon suggests the potential presence of trapped seismic energy within geothermal conduits or dykes, which could resonate and generate the observed coda wave (Neuberg et al., 2006; Benson et al., 2008; Burlini and Di Toro, 2008).

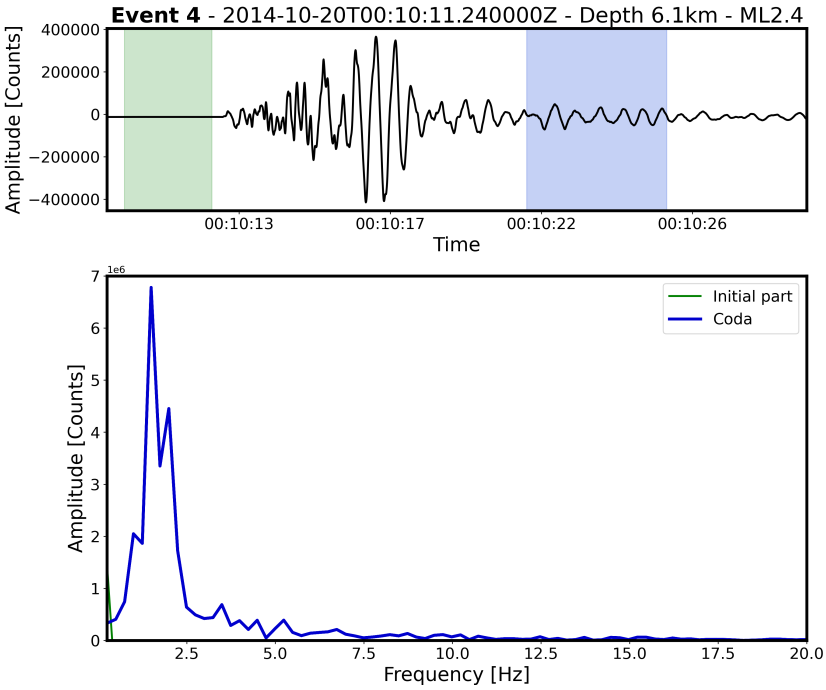

Figure 4.8. Seismic waveform and frequency analysis for event 4. The top panels show the seismic signal amplitude over time, with the coda wave following the main event. The bottom panels display the frequency spectra of the signal and noise, highlighting the resonating seismic energy.

Figure 4.8 illustrates a long-period seismic event (event 4). The top panels display the amplitude of seismic signals over time, highlighting the main events followed by their respective coda waves. The green and blue shaded areas indicate time windows for noise and resonating code signal, respectively. The bottom panels present frequency analyses for these events, contrasting signal frequencies with background noise. The frequency spectra clearly distinguish the signal (blue) from noise (green), confirming the presence of resonating seismic energy (Buurmen & West, 2010).

This observation aligns with the proposed model of brittle failure of magma or fluids in volcanic environments (Neuberg et al., 2006). Similar behaviours have been observed where energy becomes trapped and resonates within conduits, contributing to extended coda waves (see experimental examples in Benson et al., 2008; Burlini and Di Toro, 2008). Models for these extended low-frequency codas include resonating hydrothermal fractures (Chouet, 1988). This concept parallels the movement of geothermal fluids within conduits in geothermal fields, where fluid dynamics may similarly influence seismic activity.

4.3.5 Hybrid-type earthquake

Hybrid earthquakes are characterized by an initial high-frequency onset followed by a low-frequency coda, reflecting a complex interaction between seismic dynamics and fluid processes within geothermal systems, according to Harrington and Brodsky (2007). Figure 4.9 and 4.10 show earthquakes in this study that exhibit an initial phase with high frequencies similar to regular earthquakes, followed by a coda phase characterized by a more resonant nature, suggesting they are hybrid earthquakes.

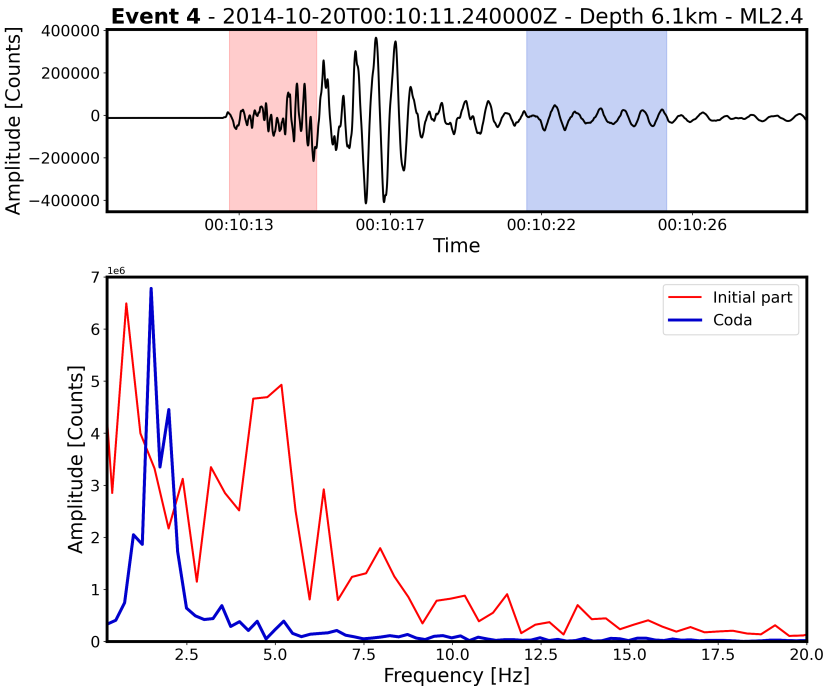

Figure 4.9. Seismic waveform of a long-period earthquake for event 4. The plot highlights the spectral comparison between the initial high-frequency part and the resonant coda part of the earthquake.

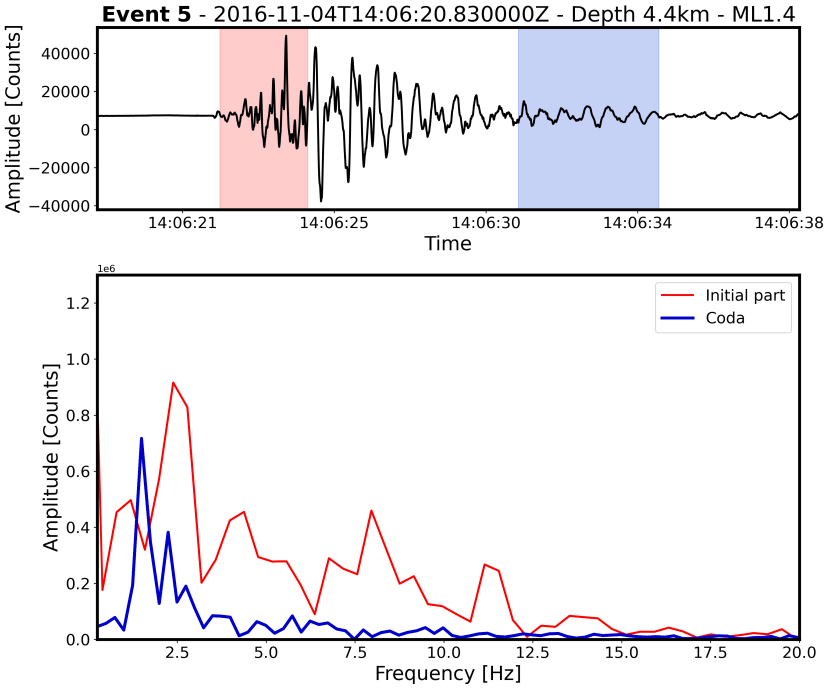

Figure 4.10. Seismic waveform of a long-period earthquake for event 5. The plot highlights the spectral comparison between the initial high-frequency part and the resonant coda part of the earthquake.

The hybrid waveform identified in this study corresponds to the findings of Harrington and Brodsky (2007), who stated that the low-frequency component of hybrid waveforms can be attributed to either the presence of fluids within the geological medium or the effects of seismic waves traversing intricate pathways and geological structures. Additionally, Buurman and West (2010) proposed that hybrid earthquakes result from the interaction between ascending magmatic fluids and the brittle crust.

4.4 Corner frequency estimation

Corner frequency estimation is crucial in seismic analysis for assessing stress drop ($\Delta\sigma$), a key parameter in earthquake dynamics and hazard assessment (Madariaga, 1976). In this study, spectral fitting was applied to 13 selected long-period seismic events to estimate corner frequencies by analysing the decay of spectral amplitudes with frequency (Figure 2.2 and 2.3). Figure 4.11 shows the plot of the relationship between corner frequency and seismic moment for these 13 long-period events. The plot reveals that all events are clustered below 1 MPa in stress drop. Lower corner frequencies typically indicate lower stress drops, reflecting a relatively smoother spectrum of seismic energy release (Madariaga, 1976).

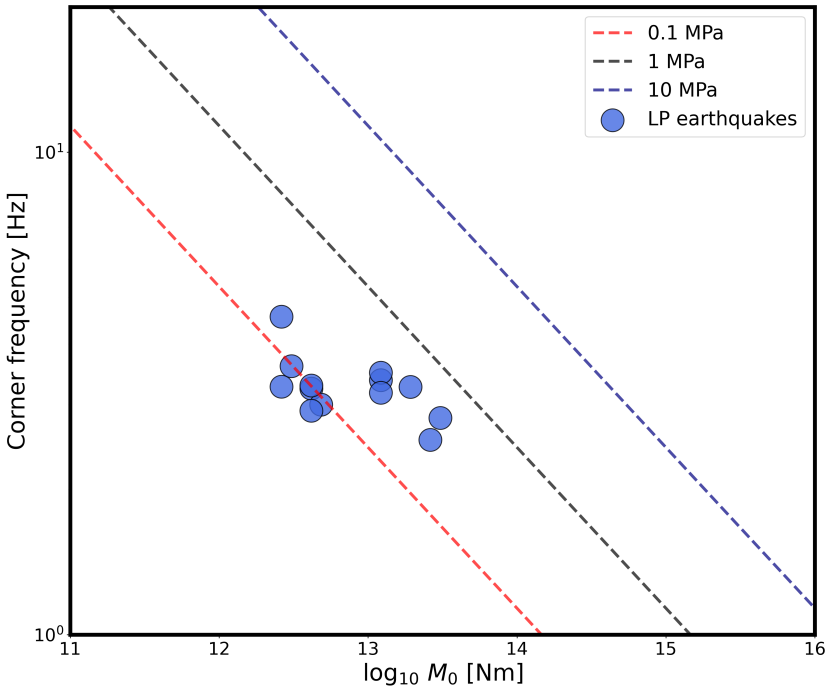

Figure 4.11. Corner frequency scaling versus seismic moment. The lines represent constant stress-drop relationships. Blue circles indicate long-period events.

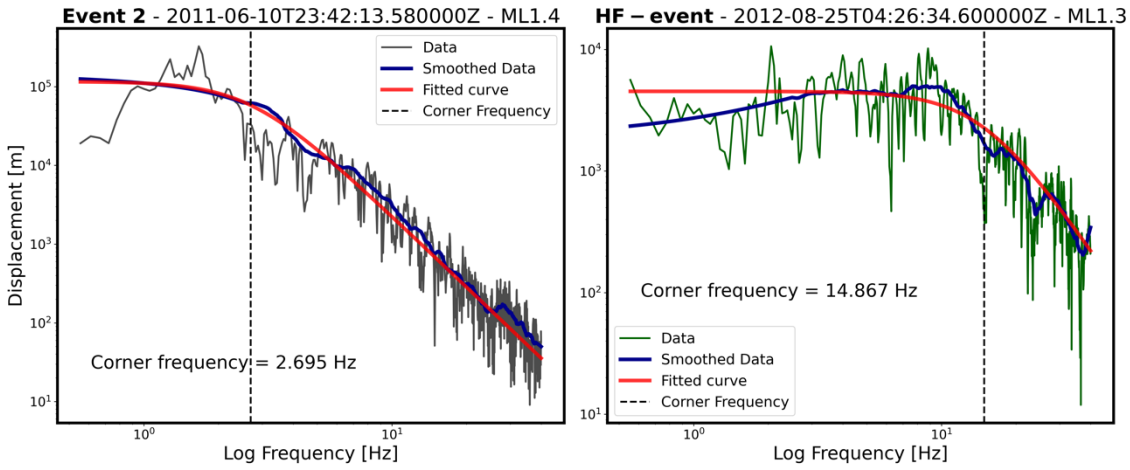

Figure 4.11. Comparison of corner frequency estimation for two earthquakes with similar magnitude (ML) and located at the same location. (left) shows long-period earthquake (event 2) and (right) is the corner frequency estimation for regular earthquake (high-frequency).

While most long-period events show relatively low corner frequencies, accurately estimating corner frequencies for high-frequency earthquakes was challenging and often largely impossible (see Figure 4.11). Rapid amplitude decay, high noise levels, and indistinct transition points posed significant challenges in spectral data fitting. Addressing these issues may require alternative approaches to improve the reliability of spectral analysis for high-frequency seismic events. Recent studies highlight the complex spectral characteristics of high-frequency seismic signals due to attenuation effects and noise levels (Bostock et al., 2017). This complexity underscores the need for advanced methodologies to accurately determine corner frequencies and assess stress drop in such events. In conclusion, corner frequencies were successfully estimated only for long-period events due to these challenges.

4.5 Stress drop analysis

In this study, stress drop values for the selected 13 long-period earthquakes within the Larderello-Travale geothermal field consistently fall below 1 MPa, which is significantly lower than the global range of 1 to 100 MPa (Kanamori and Brodsky, 2004). These stress drop values may be related to the unique geological and operational conditions prevailing in the geothermal field. Factors such as fluid injection and extraction processes might influence the fault stress state by altering the fluid pressure, which reduces the effective normal stress on the faults. This reduction in effective normal stress can facilitate fault slip, potentially increasing the frequency of smaller, low-stress-drop earthquakes (Brodsky & Mori, 2007). Thus, these processes may contribute to the occurrence of more frequent, smaller seismic events with lower stress drops.

The lower stress drop values observed in this study can be attributed to the nature of long-period earthquakes. Long-period earthquakes typically have lower stress drops because they are associated with slow slip events, which involve gradual and smooth fault movements (Ide et al., 2007; Wang et al., 2023). In the context of the Larderello-Travale geothermal field, these seismic

behaviours are influenced by both the area's geological structure and operational practices. For instance, Goertz-Allmann et al. (2011) noted varying stress drop levels across different locations, with lower stress drops near injection sites, indicating a pattern of earthquake migration concurrent with fluid movement. The geothermal field's complex fault systems and high permeability zones facilitate fluid migration (Bertini et al., 2006). Moreover, activities like fluid extraction and injection alter fault zone fluid pressures, thereby reducing effective normal stress and attenuating stress buildup. These geological and operational factors collectively contribute to the occurrence of long-period earthquakes with lower stress drops (Jousset et al., 2010).

As discussed in Chapter 2 stress drop for each long-period event was estimated using local magnitudes (M_L) converted to moment magnitudes (M_w), and subsequently determining seismic moments (M_0). By integrating these data with corner frequencies (f_c), I derived source radius (r), enabling the computation of stress drops ($\Delta\sigma$) (See methods section 2.6). The observed trend in stress drop ($\Delta\sigma$) values, increasing with moment magnitude (M_w) (Figure 3.16 in chapter 3), suggests that larger seismic events within the geothermal field exhibit more distributed and more stress release (Paul & Hazarika, 2022). In summary, geothermal activities, including fluid injection and extraction, likely contribute to smoother fault movements and lower stress accumulation, which are characteristic of long-period earthquakes in geothermal environments (e.g., Frank et al., 2018; Jousset et al., 2010).

Chapter 5

Conclusion and future work

5.1 Conclusion and summary

This study represents a pioneering effort in identifying and characterizing long-period earthquakes within the Larderello-Travale geothermal field. I successfully identified 13 long-period earthquakes from 1,577 seismic events detected by the TRIF station between 2011 and 2024, utilising a frequency index threshold of 1.25. This is the first ever documentation of such events in Italy.

Spectral fitting techniques revealed that the identified long-period earthquakes possess lower corner frequencies and stress drops (ranging from 0.012 MPa to 0.089 MPa) compared to the global range for typical earthquakes (1 MPa to 100 MPa). The unique geological features of the Larderello-Travale field, including complex fault systems and high permeability zones, coupled with geothermal operations such as fluid extraction and injection, may play a role in influencing seismic activity. These factors likely contribute to the occurrence of long-period earthquakes by altering fluid pressures and facilitating smoother fault slip (e.g., Fujita & Ida, 2003).

The spatial distribution of these earthquakes (Figure 4.3) shows a concentration near geothermal infrastructures, suggesting a possible link to anthropogenic activities in the geothermal area. However, the temporal randomness of these events indicates that they are not solely triggered by scheduled geothermal operations, implying a combination of both natural and anthropogenic influences. This complexity underscores the need for further investigation into the exact mechanisms driving these events.

The methodology used in this study provides a successful framework for identifying and characterizing long-period earthquakes, which can be applied to other geothermal regions. The spatial and depth distributions of these earthquakes offer insights into how geothermal operations might trigger or influence seismic events. Future research should incorporate independent data, such as the evolution of fluid pressure from injection activities, to further clarify the relationship between geothermal operations and long-period earthquakes.

In conclusion, this study illuminates the seismic behaviour of the Larderello-Travale geothermal field, demonstrating the intricate interaction between geological features and geothermal activities. The identification of 13 long-period earthquakes represents a significant advancement in seismic research within the Larderello-Travale geothermal field. These findings are pivotal for enhancing earthquake risk assessments and promoting sustainable management of geothermal resources. Moreover, they provide a strong foundation for future research in this area.

5.2 Limitations and future study

While this study provides valuable insights into the seismic characteristics of the Larderello-Travale geothermal field, one limitation is the focus on only 13 out of 51 identified low-frequency events that are within a 15 km radius of the TRIF station. This limited coverage may not fully represent the diversity of low-frequency seismic activity across the geothermal field. Given the scope of the present research, events occurring beyond this range (refer to figure 3.1) were not studied, potentially overlooking important seismic patterns and dynamics in more distant areas.

To address the current limitations and advance understanding in this field, future research should pursue several key directions. Firstly, conducting an extended spatial analysis that goes beyond the 15 km radius from the TRIF station is crucial. This broader survey could involve data use from more than one

seismic station to enhance spatial resolution and capture a more comprehensive view of seismic activity throughout the Larderello-Travale geothermal field. Secondly, improving data processing methods is essential, particularly for handling challenges associated with high-frequency seismic events. Lastly, integrating multi-disciplinary data sources such as geodetic, geochemical, and hydrological datasets will enable researchers to explore complex correlations and interactions between geothermal operations and seismicity, providing deeper insights into the underlying mechanisms driving seismic activity in geothermal fields. These approaches collectively aim to refine seismic monitoring capabilities and contribute to more effective management practices for geothermal energy resources.

Appendix: Code

The following Python code is used to obtain the Frequency Index (FI) for each earthquake:

```
#!/usr/bin/env python3
# -*- coding: utf-8 -*-
"""
Created on Wed Jul  3 13:07:33 2024

@author: chulalak
"""
import obspy
import numpy as np
from obspy import UTCDateTime
import matplotlib.pyplot as plt
import matplotlib.dates as mdates
from obspy import read
from obspy.geodetics import locations2degrees

# Read data
file_path = ## Path to .mseed file
st = read(file_path)
event_time = UTCDateTime('2011-01-04T06:25:16.050000') # from event excel file
event_lat = 43.192
event_lon = 10.899
event_depth = 10.1
ML = 1.5

# TRIF location
sta_lat = 43.11478
sta_lon = 10.90265

# Calculation
```

```
event_dist  = locations2degrees(event_lat, event_lon, sta_lat, sta_lon)
model = obspy.taup.TauPyModel('iasp91')
t_p = model.get_travel_times(source_depth_in_km=event_depth,
distance_in_degree=event_dist, phase_list=["ttp+"])

# Trimming
origin_time = event_time
arrival_time = origin_time + t_p[0].time - 2 # p phase
starttime = arrival_time
endtime = starttime + 18 #### Adjust here
st_trim = st.copy()
st_trim.trim(starttime, endtime)

# Spectrum
tr = st_filt[0]
data = tr.data
sampling_rate = tr.stats.sampling_rate
spec = np.fft.fft(data)
freq = np.fft.fftfreq(len(data), d=1/sampling_rate)

# Calculate FI
f_lf = np.where((freq > 1) & (freq < 5))[0]
f_hf = np.where((freq > 5) & (freq < 10))[0]
FI = sum(np.abs(spec[f_lf])) / sum(np.abs(spec[f_hf]))

# Ploting

fig, axs = plt.subplots(2, 1, figsize=(12, 10), dpi=300)

# Plot st_trim
axs[0].plot(st_trim[0].times("matplotlib"), st_trim[0].data, color='black', label='Trimmed',
linewidth=2)
axs[0].set_ylabel('Amplitude', fontsize=16)
axs[0].set_title('2011-01-04T06:25:16.050000 : Depth 10.1 km : ML1.5', fontsize=22)
axs[0].set_title(f'{event_time}, Depth={event_depth}km, ML{ML}', fontsize = 22)
```

```
axs[0].set_xlim(st_trim[0].times("matplotlib")[0], st_trim[0].times("matplotlib")[-1])
axs[0].xaxis.set_major_formatter(mdates.DateFormatter('%H:%M:%S'))
axs[0].xaxis.set_major_locator(mdates.SecondLocator(interval=4))
axs[0].tick_params(axis='both', labelsize=18)  # Increase font size of x-axis tick labels

# Plot spectrum
axs[1].semilogy(np.abs(freq), np.abs(spec), color='black', linewidth=2)
axs[1].axvspan(freq[f_lf[0]], freq[f_lf[-1]], color='royalblue', alpha=0.5, label='LF Zone')
axs[1].axvspan(freq[f_hf[0]], freq[f_hf[-1]], color='red', alpha=0.3, label='HF Zone')
axs[1].set_xscale('log') ## Plot x-axis with log scale
axs[1].set_xlim(freq[0],freq[300])

# Calculate midpoints of LF and HF zones
lf_midpoint_freq = np.mean([freq[f_lf[0]], freq[f_lf[-1]]])
hf_midpoint_freq = np.mean([freq[f_hf[0]], freq[f_hf[-1]]])

# Place text in the middle of LF and HF zones for the bottom subplot
axs[1].text(lf_midpoint_freq, min(np.abs(spec))/0.5, 'LF Zone', color='black',
fontsize=18, ha='center', va='top')
axs[1].text(hf_midpoint_freq, min(np.abs(spec))/0.5, 'HF Zone', color='black',
fontsize=18, ha='center', va='top')

axs[1].text(freq[2], max(np.abs(spec)), f'FI = {FI:.2f}', color='black', fontsize=22,
ha='right', va='top')
axs[1].set_xlabel('Frequency (log)', fontsize=18)
axs[1].set_ylabel('Amplitude (log)', fontsize=18)
axs[1].tick_params(axis='both', labelsize=18)  # Increase font size of both axes tick
labels

plt.tight_layout()
plt.show()
```

The following Python code is used to obtain the corner frequency estimation by spectral fitting technique of the different signals recorded by each station for each earthquake:

```
#!/usr/bin/env python3
# -*- coding: utf-8 -*-
"""
Created on Mon Jul  1 22:17:56 2024
@author: chulalak
"""
#!/usr/bin/env python3
# -*- coding: utf-8 -*-
import numpy as np
import matplotlib.pyplot as plt
from scipy.optimize import curve_fit
from obspy import read, UTCDateTime
from obspy.taup import TauPyModel
from obspy.geodetics import locations2degrees
from scipy.signal import savgol_filter

# Define Brune function
def brune_f(f, omega_0, f_c, Q):
    n = 3           # original = 2
    gamma = 1   # original =1
    t = 0
    return (omega_0 * np.exp(-np.pi * f * t / Q)) / ((1 + (f / f_c) ** (gamma * n)) ** (1 / gamma))

# Read data
file_path =  # Path to .mseed file
st = read(file_path)
event_time = UTCDateTime('2012-07-26T20:43:29.140000')
event_lat, event_lon, event_depth, ML = 43.1447, 10.8663, 7.3, 1.4
sta_lat, sta_lon = 43.11478, 10.90265
```

```
# Distance and time calculation
event_distance = locations2degrees(event_lat, event_lon, sta_lat, sta_lon)
model = TauPyModel('iasp91')
t_p = model.get_travel_times(source_depth_in_km=event_depth,
distance_in_degree=event_distance, phase_list=["ttp+"])

# Trim signal
starttime = event_time + t_p[0].time - 2
endtime = starttime + 18
event_trim = st.copy().trim(starttime, endtime)

# Compute spectrum
tr = event_trim[0]
data = tr.data
sampling_rate = tr.stats.sampling_rate
freq = np.fft.fftfreq(len(data), d=1 / sampling_rate)
spec = np.fft.fft(data)
with np.errstate(divide='ignore', invalid='ignore'):
    spec = np.where(freq == 0, 0, spec / (2 * np.pi * freq))
fft_amplitudes = np.abs(spec)
positive_freq_mask = freq > 0
freq = freq[positive_freq_mask] # Only positive frequency
fft_amplitudes = fft_amplitudes[positive_freq_mask]

# Frequency range for fitting
freq_mask = (freq >= 0.3) & (freq <= 50)
freq_fit = freq[freq_mask]
fft_amplitudes_fit = fft_amplitudes[freq_mask]

# Smoothing
window_length = min(60, len(fft_amplitudes_fit) - 1)
if window_length % 2 == 0:
    window_length += 11
smoothed_fft_amplitudes = savgol_filter(fft_amplitudes_fit,
window_length=window_length, polyorder=1)
```

```
# Grid search for f_c
f_c_values = np.linspace(0.1, 20)
best_f_c, best_score = None, float('-inf')
for f_c in f_c_values:
    p0 = [0.1, f_c, 0.1]
    params, _ = curve_fit(brune_f, freq_fit, smoothed_fft_amplitudes, p0=p0)
    score = -np.mean((smoothed_fft_amplitudes - brune_f(freq_fit, *params)) ** 2)
    if score > best_score:
        best_score, best_f_c = score, f_c

# Fit the model with the best f_c value
p0 = [0.1, best_f_c, 0.1]
params, _ = curve_fit(brune_f, freq_fit, smoothed_fft_amplitudes, p0=p0)
Omega_0_fit, f_c_fit, Q_fit = params

# Calculate M0
Mw = ((2 / 3) * ML) + 1.14
M0 = 10 ** (Mw - (-10.545))
K, Vs = 0.32, 2700
Vp = 1.73 * Vs

# Calculate r and stress drop
r = (K * Vp) / f_c_fit
S = ((7 / 16) * (M0 / r ** 3)) / 10 ** 6

# Plotting
plt.figure(figsize=(11, 8), dpi=300)
plt.loglog(freq[freq_mask], fft_amplitudes[freq_mask], color='navy', alpha=0.7,
label='Data', linewidth=2)
plt.loglog(freq_fit, smoothed_fft_amplitudes, label='Smoothed Data', color='darkblue',
linewidth=4)
plt.loglog(freq_fit, brune_f(freq_fit, *params), color='orange', alpha=0.8, label='Fitted
curve', linewidth=4)
plt.text(1 * freq[freq_mask][1], 0.00003 * fft_amplitudes[freq_mask][1], f'Corner
frequency = {params[1]:.3f} Hz', fontsize=20, color='black')
```

```
plt.xlabel('Log Frequency [Hz]', fontsize=20)
plt.ylabel('Displacement [m]', fontsize=20)
plt.axvline(x=params[1], color='black', linestyle='--', label='Corner Frequency',
linewidth=2)
plt.title(f'{event_time} - ML{ML}', fontsize=22)
plt.tick_params(axis='both', labelsize=14)
plt.legend(fontsize=16)
ax = plt.gca()
for spine in ax.spines.values():
    spine.set_linewidth(3)
plt.show()
```

Appendix: Figures

The following figures are the selected 13 long-period earthquakes with the time window of 18 seconds (2 seconds before and 18 seconds after p-arrival):

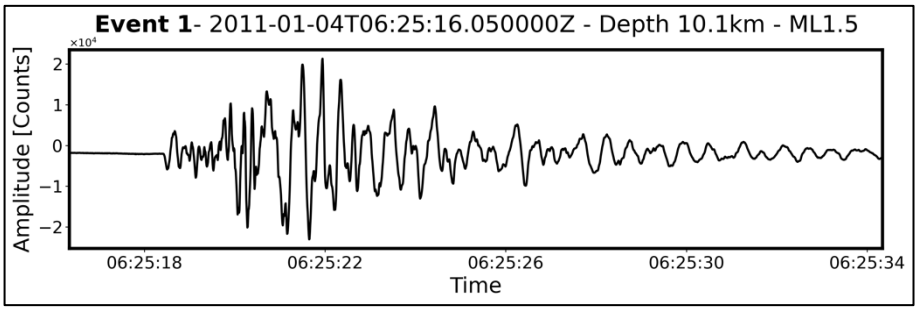

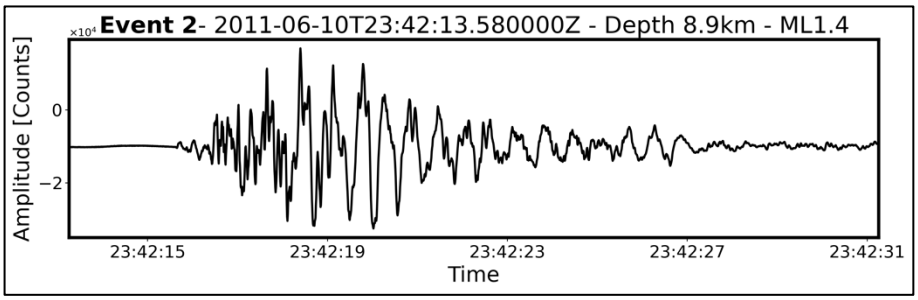

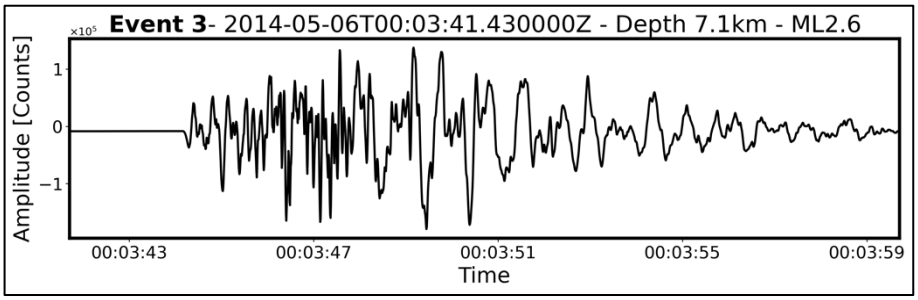

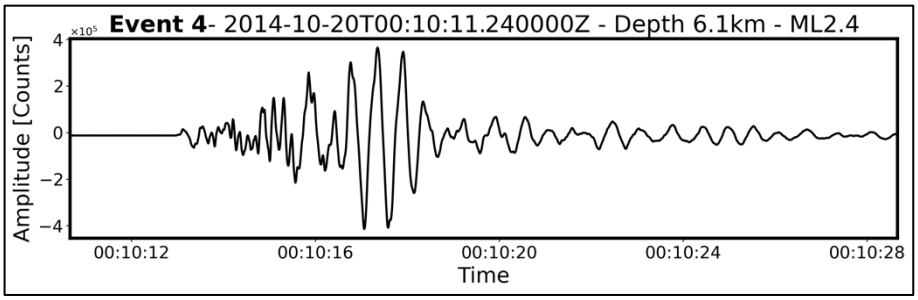

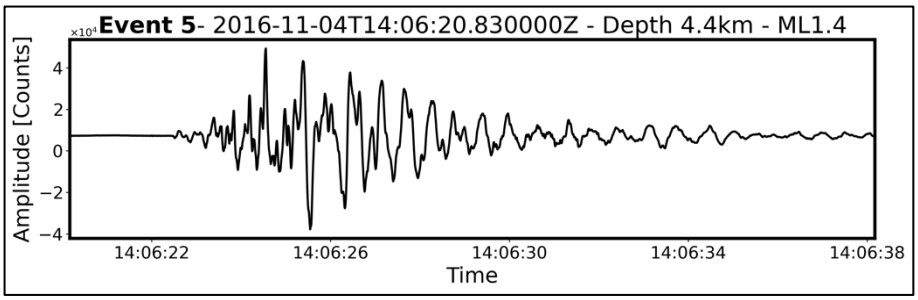
Event 5- 2016-11-04T14:06:20.830000Z - Depth 4.4km - ML1.4
×10⁴
Amplitude [Counts]
4
2
0
−2
−4
14:06:22
14:06:26
14:06:30
14:06:34
14:06:38
Time

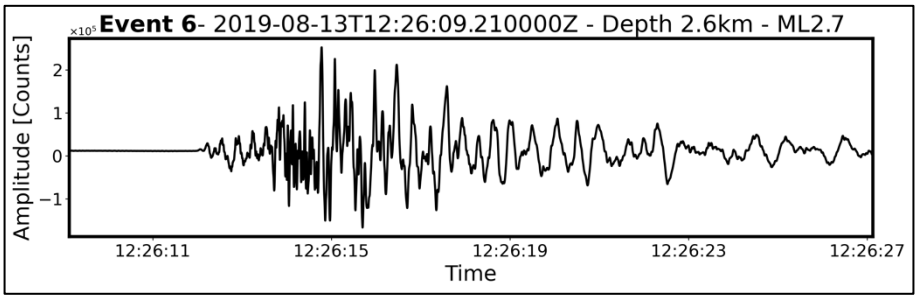
Event 6- 2019-08-13T12:26:09.210000Z - Depth 2.6km - ML2.7
×10⁵
Amplitude [Counts]
2
1
0
−1
12:26:11
12:26:15
12:26:19
12:26:23
12:26:27
Time

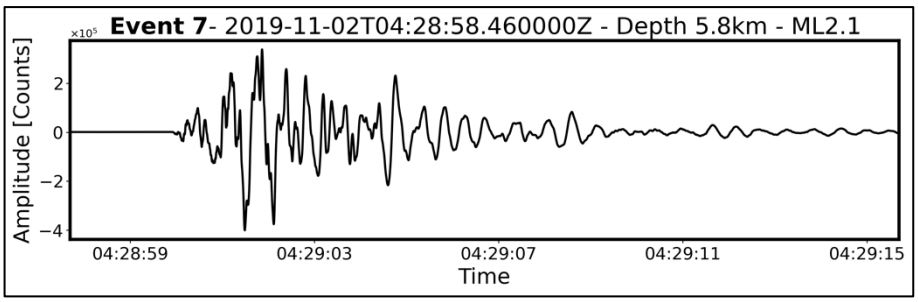
Event 7- 2019-11-02T04:28:58.460000Z - Depth 5.8km - ML2.1
×10⁵
Amplitude [Counts]
2
0
−2
−4
04:28:59
04:29:03
04:29:07
04:29:11
04:29:15
Time

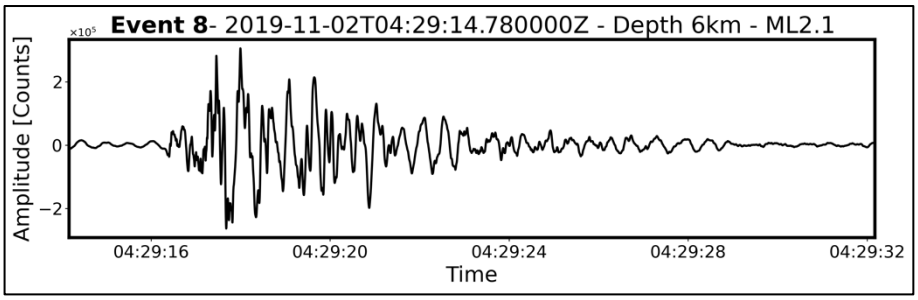
Event 8- 2019-11-02T04:29:14.780000Z - Depth 6km - ML2.1
×10⁵
Amplitude [Counts]
2
0
−2
04:29:16
04:29:20
04:29:24
04:29:28
04:29:32
Time

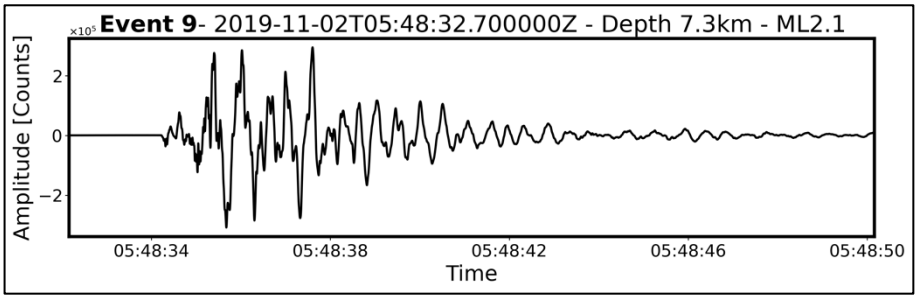
Event 9- 2019-11-02T05:48:32.700000Z - Depth 7.3km - ML2.1
×10⁵
Amplitude [Counts]
2
0
−2
05:48:34
05:48:38
05:48:42
05:48:46
05:48:50
Time

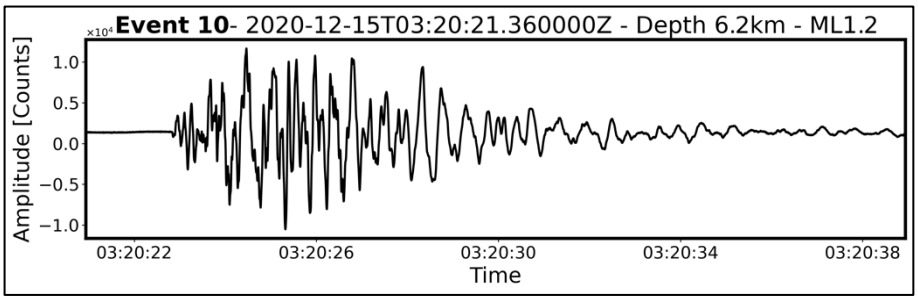
Event 10- 2020-12-15T03:20:21.360000Z - Depth 6.2km - ML1.2
×10⁴
1.0
0.5
0.0
−0.5
−1.0
Amplitude [Counts]
03:20:22
03:20:26
03:20:30
03:20:34
03:20:38
Time

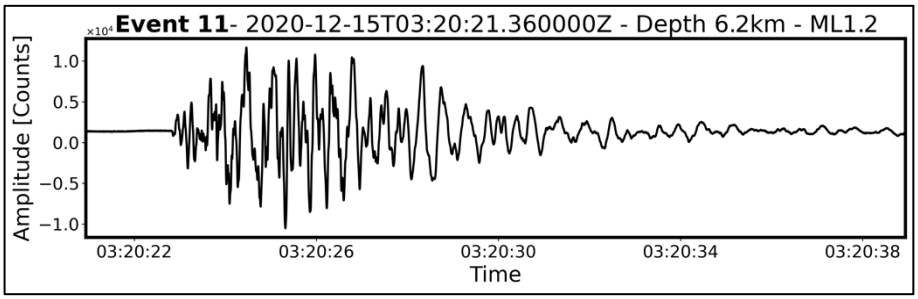
Event 11- 2020-12-15T03:20:21.360000Z - Depth 6.2km - ML1.2
×10⁴
1.0
0.5
0.0
−0.5
−1.0
Amplitude [Counts]
03:20:22
03:20:26
03:20:30
03:20:34
03:20:38
Time

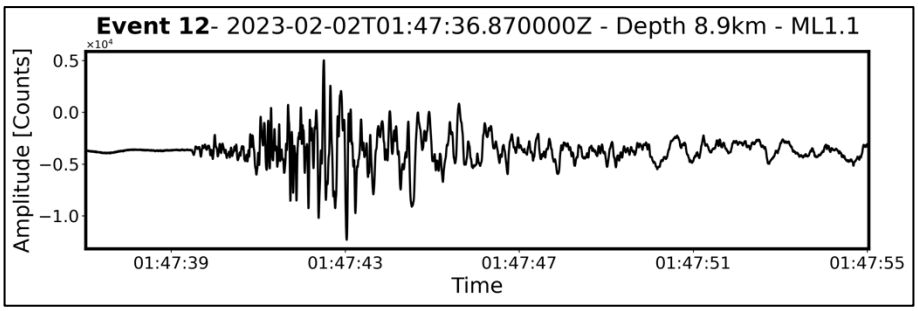
Event 12- 2023-02-02T01:47:36.870000Z - Depth 8.9km - ML1.1
×10⁴
0.5
0.0
−0.5
−1.0
Amplitude [Counts]
01:47:39
01:47:43
01:47:47
01:47:51
01:47:55
Time

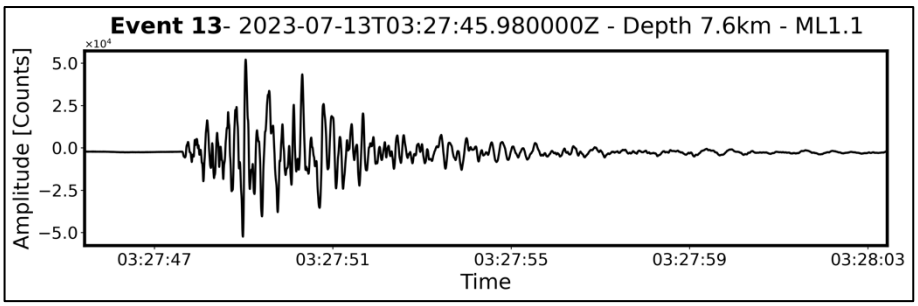
Event 13- 2023-07-13T03:27:45.980000Z - Depth 7.6km - ML1.1
×10⁴
5.0
2.5
0.0
−2.5
−5.0
Amplitude [Counts]
03:27:47
03:27:51
03:27:55
03:27:59
03:28:03
Time

The spectral fitting and corner frequency estimation for each long-period earthquake will be displayed in this appendix. Each figure show the event number, origin time and magnitude of the earthquake on the top. In each plot, data, smoothed data, fitted curve, and corner frequency are shown:

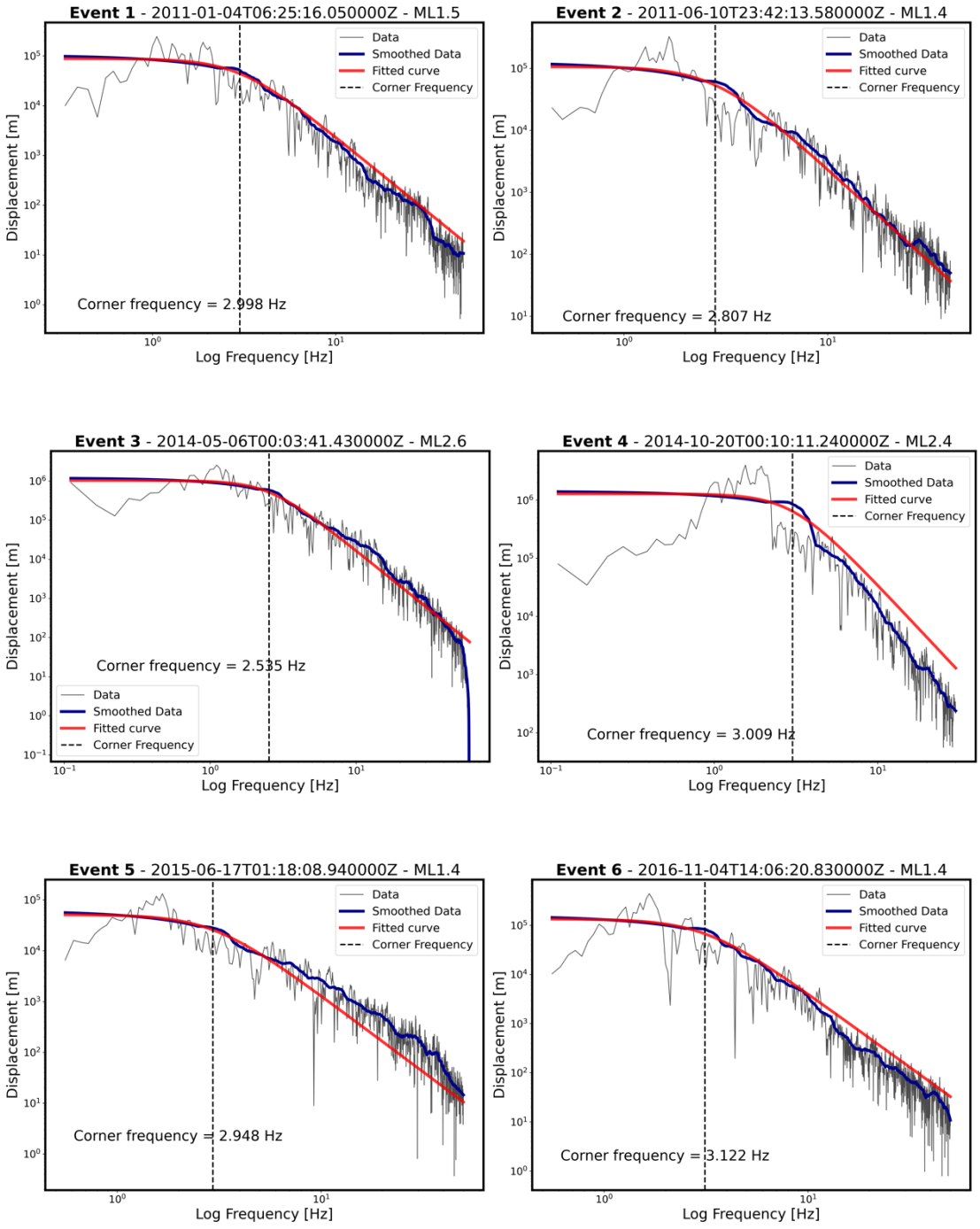

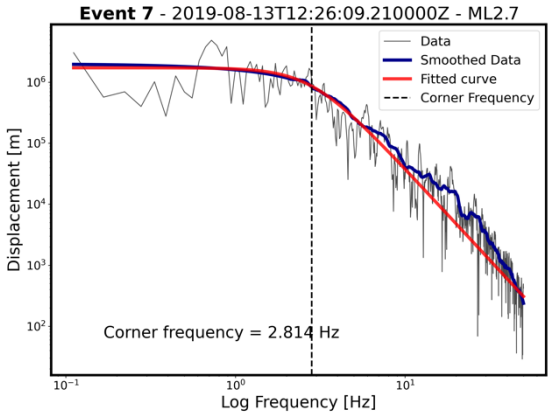
Event 7 - 2019-08-13T12:26:09.210000Z - ML2.7
Data
Smoothed Data
Fitted curve
Corner Frequency
Displacement [m]
Corner frequency = 2.814 Hz
Log Frequency [Hz]

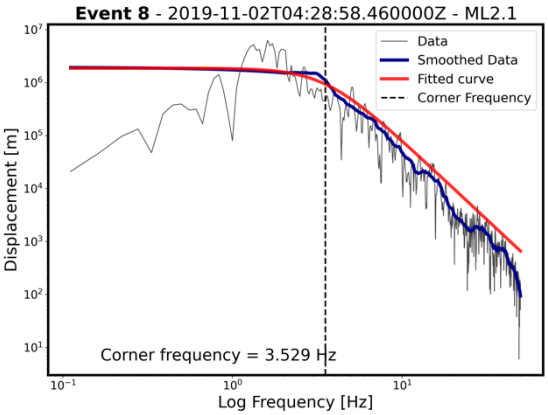
Event 8 - 2019-11-02T04:28:58.460000Z - ML2.1
Data
Smoothed Data
Fitted curve
Corner Frequency
Displacement [m]
Corner frequency = 3.529 Hz
Log Frequency [Hz]

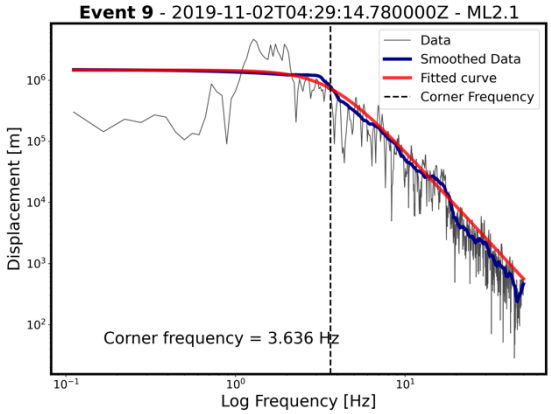
Event 9 - 2019-11-02T04:29:14.780000Z - ML2.1
Data
Smoothed Data
Fitted curve
Corner Frequency
Displacement [m]
Corner frequency = 3.636 Hz
Log Frequency [Hz]

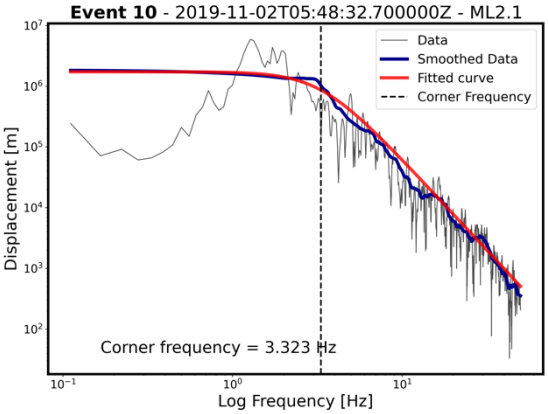
Event 10 - 2019-11-02T05:48:32.700000Z - ML2.1
Data
Smoothed Data
Fitted curve
Corner Frequency
Displacement [m]
Corner frequency = 3.323 Hz
Log Frequency [Hz]

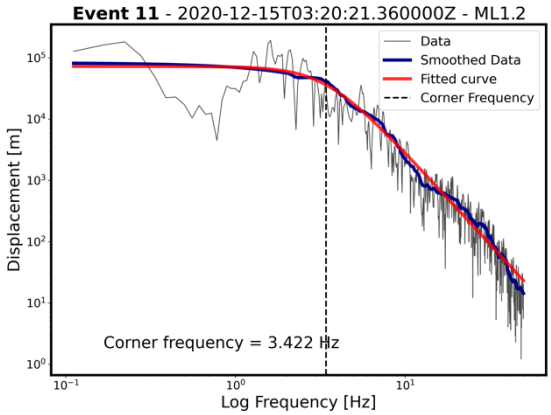
Event 11 - 2020-12-15T03:20:21.360000Z - ML1.2
Data
Smoothed Data
Fitted curve
Corner Frequency
Displacement [m]
Corner frequency = 3.422 Hz
Log Frequency [Hz]

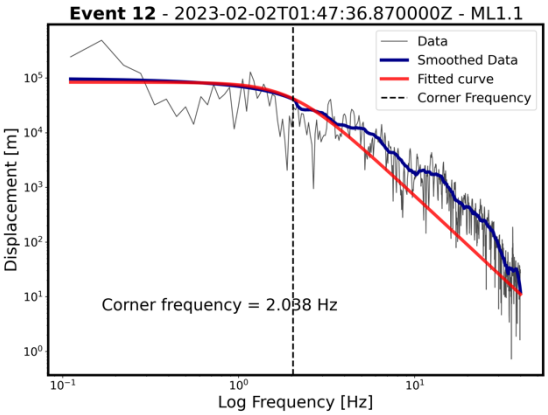
Event 12 - 2023-02-02T01:47:36.870000Z - ML1.1
Data
Smoothed Data
Fitted curve
Corner Frequency
Displacement [m]
Corner frequency = 2.038 Hz
Log Frequency [Hz]

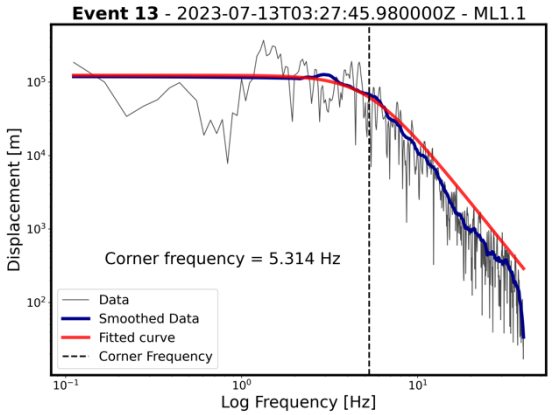
Event 13 - 2023-07-13T03:27:45.980000Z - ML1.1
Displacement [m]
Log Frequency [Hz]
Corner frequency = 5.314 Hz
Data
Smoothed Data
Fitted curve
Corner Frequency

References

Abercrombie, R. E. (1995). Earthquake source scaling relationships from −1 to 5 ML, using seismograms recorded at 2.5 km depth. Journal of Geophysical Research, 100, 24015–24036.

Agurto-Detzel, H., Bianchi, M., Prieto, G. A., & Assumpção, M. (2017). Earthquake source properties of a shallow induced seismic sequence in SE Brazil. Journal of Geophysical Research, 122, 2784–2797. https://doi.org/10.1002/2016JB013623

Arias, A., Dini, I., Casini, M., Fiordelisi, A., Perticone, I., & Dell'Aiuto, P. (2010). Geoscientific Feature Update of the Larderello-Travale Geothermal System (Italy) for a Regional Numerical Modeling. In Proceedings World Geothermal Congress 2010, Bali, Indonesia, 25-29 April 2010. Enel Green Power.

Audet, P., Bostock, M. G., Christensen, N. I., & Peacock, S. M. (2009). Seismic evidence for overpressured subducted oceanic crust and megathrust fault sealing. Nature, 457, 76–78. https://doi.org/10.1038/nature07650

Bagagli, M., Kissling, E., Piccinini, D., & Saccorotti, G. (2020). Local earthquake tomography of the Larderello-Travale geothermal field. Geothermics, 83, 101731. https://doi.org/10.1016/j.geothermics.2019.101731

Baldi, P., Bellani, S., Ceccarelli, A., Fiordelisi, A., Squarci, P., & Taffi, L. (1995). Geothermal anomalies and structural features of southern Tuscany. In World Geothermal Congress Proceedings (pp. 1287-1291). Florence, Italy, May 1995.

Batini, F., Bertini, G., Gianelli, G., Pandeli, E. and Puxeddu, M.. Deep structure of the Larderello field: contribution from recent geophysical and geological data. Soc. Geol. Ital. Mem., 1983; 25, 219–23

Batini, F., Brogi, A., Lazzarotto, A., Liotta, D., & Pandeli, E. (2003). Geological features of Larderello-Travale and Mt. Amiata geothermal areas (southern Tuscany, Italy). Episodes, 26, 239-244. https://doi.org/10.18814/epiiugs/2003/v26i3/015

Batini, F., Console, R., & Luongo, G. (1985). Seismological study of Larderello - Travale geothermal area. Geothermics, 14(2–3), 255-272. https://doi.org/10.1016/0375-6505(85)90066-5

Baumbach, M., & Bormann, P. (2011). Determination of source parameters from seismic spectra. GFZ German Research Centre for Geosciences. https://doi.org/10.2312/GFZ.NMSOP-2_EX_3.4

Benson, P. M., Vinciguerra, S., Meredith, P. G., & Young, R. P. (2008). Laboratory simulation of volcano seismicity. Science, 322(5899), 249-252. https://doi.org/10.1126/science.1161927

Bertini, G., Casini, M., Gianelli, G., & Pandeli, E. (2006). Geological structure of a long-living geothermal system, Larderello, Italy. Terra Nova, 18(3), 163-169. https://doi.org/10.1111/j.1365-3121.2006.00676.x

Bertani, R. (2007). World Geothermal Generation in 2007. In Proceedings of the European Geothermal Congress, Unterhaching, Germany.

Bertani, R., Bertini, G., Cappetti, G., Fiordelisi, A., & Marocco, B. M. (2005). An update of the Larderello-Travale/Radicondoli deep geothermal system. In Proceedings of the World Geothermal Congress 2005, April 24-29, 2005, Antalya, Turkey (pp. 1-6).

Boatwright, J. (1984). The effect of rupture complexity on estimates of source size. J. Geophys. Res. 89, No. B2, pp. 1132–1146.
Bolt, B. A. (2024, June 28). earthquake. Encyclopedia Britannica. https://www.britannica.com/science/earthquake-geology

Bostock, M. G., Royer, A. A., Hearn, E. H., & Peacock, S. M. (2012). Low frequency earthquakes below southern Vancouver Island. Geochemistry, Geophysics, Geosystems, 13, Q11007. https://doi.org/10.1029/2012GC004391

Bostock, M. G., Thomas, A. M., Rubin, A. M., & Christensen, N. I. (2017). On corner frequencies, attenuation, and low-frequency earthquakes. Journal of Geophysical Research: Solid Earth, 122. https://doi.org/10.1002/2016JB013405

Brodsky, E. E., & Mori, J. (2007). Creep events slip less than ordinary earthquakes. Geophysical Research Letters, 34(16).

Brogi, A., Lazzarotto, A., Liotta, B., & Ranalli, G. (2003). Extensional shear zones as imaged by reflection seismic lines: The Larderello geothermal field (central Italy). Tectonophysics, 363, 127–139.

Brogi, Andrea & Cerboneschi, Alessio. (2012). Upper crust “boudinage” during post-collisional Miocene extension in Tuscany: Insights from the southern part of the Larderello geothermal area (Northern Apennines, Italy). Geodinamica Acta. October 2007. 327-351. 10.3166/ga.20.327-351.

Brune, J. N. (1970). Tectonic stress and the spectra of seismic shear waves from earthquakes. Journal of Geophysical Research, 75(26), 4997–5009. https://doi.org/10.1029/JB075i026p04997

Burlini, L., & Di Toro, G. (2008). Volcanic symphony in the lab. Science, 322. Retrieved from https://www.sciencemag.org, DOI: 10.1126/science.1164545

Buonasorte, G., Cataldi, R., & Passaleva, G. (2007). Geothermal development in Italy: From present to future. In Proceedings of the European Geothermal Congress, Unterhaching, Germany.

Buurman, H., & West, M. (2010). Seismic precursors to volcanic explosions during the 2006 eruption of Augustine Volcano. The 2006 Eruption of Augustine Volcano, 1769.

Carella, M., Fulignati, P., Musumeci, G., & Sbrana, A. (2000). Metamorphic consequences of Neogene thermal anomaly in the northern Apennines (Radicondoli – Travale area, Larderello geothermal field, Italy). Geodinamica Acta, 13, 345–366.

Chamberlain, C. J., Shelly, D. R., Townend, J., & Stern, T. A. (2014). Low-frequency earthquakes reveal punctuated slow slip on the deep extent of the Alpine Fault, New Zealand. Geochemistry, Geophysics, Geosystems, 15, 2984–2999. https://doi.org/10.1002/2014GC005436

Clarke, J., Adam, L., & van Wijk, K. (2021). LP or VT signals? How intrinsic attenuation influences volcano seismic signatures constrained by Whakaari volcano parameters. Journal of Volcanology and Geothermal Research, 418, 107337. https://doi.org/10.1016/j.jvolgeores.2021.107337

Chu, R., & Sheng, M. (2023). Stress features inferred from induced earthquakes in the Weiyuan Shale gas block in Southwestern China. Journal of Geophysical Research, 128, 1–14.

Decandia, F. A., Lazzarotto, A., & Liotta, D. (2001). Structural features of southern Tuscany, Italy. Ofioliti, 26, 287–300.

Del Moro, A., Pardelli, G., Quercioli, C., Villa, I. M., & Callegari, E. (1982). Rb/Sr and K/Ar chronology of the southern Tuscany magmatic province, Italy: Miocene-Pliocene plutons. Contributions to Mineralogy and Petrology, 81(2), 142-151.

Ellsworth, W.L., Giardini, D., Townend, J., Ge, S., & Shimamoto, T. (2019). Triggering of the Pohang, Korea, earthquake (Mw 5.5) by enhanced geothermal system stimulation. Seismological Research Letters, 90(5), 1844–1858.

Elter, P., & Pandeli, E. (1990). Geological setting and orogenic evolution of the northern Apennines. Geological Society of America Bulletin, 102(5), 624-638.

Enel Green Power. (n.d.). Our projects. Retrieved June 17, 2024, from https://www.enelgreenpower.com/our-projects

Eshelby, J. D. (1957). The determination of the elastic field of an ellipsoidal inclusion and related problems. Proceedings of the Royal Society of London. Series A, Mathematical and Physical Sciences, 241, 376–396.

Evans, K. F., Zappone, A., Kraft, T., Deichmann, N., & Moia, F. (2012). A survey of the induced seismic responses to fluid injection in geothermal and CO2 reservoirs in Europe. Geothermics, 41, 30–54.

Eyre, T. S., C. J. Bean, L. De Barros, F. Martini, I. Lokmer, M. M. Mora, J. F. Pacheco, and G. J. Soto (2015), A brittle failure model for long-period seismic events recorded at Turrialba Volcano, Costa Rica. J. Geophys. Res. Solid Earth, 120, 1452–1472.

Farge, G., Shapiro, N. M., & Frank, W. B. (2020). Moment-duration scaling of low-frequency earthquakes in Guerrero, Mexico. Journal of Geophysical Research: Solid Earth, 125, e2019JB019099. https://doi.org/10.1029/2019JB019099

Frank, W.B., Shapiro, N.M., & Gusev, A.A. (2018). Progressive reactivation of the volcanic plumbing system beneath Tolbachik volcano (Kamchatka, Russia) revealed by long-period seismicity. Earth and Planetary Science Letters, 493, 47–56. https://doi.org/10.1016/j.epsl.2018.04.018

Frank, W. B., Shapiro, N. M., Kostoglodov, V., Husker, A. L., Campillo, M., Payero, J. S., & Prieto, G. A. (2013). Low-frequency earthquakes in the Mexican Sweet Spot. Geophysical Research Letters, 40, 2661–2666. https://doi.org/10.1002/grl.50561

Fridleifsson, I., Bertani, R., Huenges, E., Lund, J., Ragnarsson, Á., & Rybach, L. (2008). The possible role and contribution of geothermal energy to the mitigation of climate change. In IPCC Scoping Meeting on Renewable Energy Sources, Proceedings (pp. 59–80).

Fujita, Y., & Ida, Y. (2003). Geometrical effects and low-attenuation resonance of volcanic fluid inclusions for the source mechanism of long-period earthquakes. Journal of Geophysical Research, 108(1).

Gianelli, G., & Laurenzi, M. A. (2001). Radiometric dating of geothermal systems. Journal of Volcanology and Geothermal Research, 110(1-2), 67-83.

Gianelli, G., Manzella, A., & Puxeddu, M. (1997). Crustal models of the geothermal areas of southern Tuscany (Italy). Tectonophysics, 281, 221–239.

Gianelli, G., & Ruggieri, G. (2002). Evidence of a contact metamorphic aureole with high-temperature metasomatism in the deepest part of the active geothermal field of Larderello, Italy. Geothermics, 31, 443–474

Goertz-Allmann, B. P., Goertz, A., & Wiemer, S. (2011). Stress drop variations of induced earthquakes at the Basel geothermal site. Geophysical Research Letters, 38(9). https://doi.org/10.1029/2011GL047498
Greenfield, T., Keir, D., Kendall, J. M., & Ayele, A. (2019). Low-frequency earthquakes beneath Tullu Moye volcano, Ethiopia, reveal fluid pulses from shallow magma chamber. Earth and Planetary Science Letters, 526, 115782. https://doi.org/10.1016/j.epsl.2019.115782

Hanks, T. C., & Kanamori, H. (1979, May 10). A Moment magnitude scale. Journal of Geophysical Research, 84(B5), 2348–2350. https://doi.org/10.1029/JB084iB05p02348

Harrington, R. M., & Brodsky, E. E. (2007). Volcanic hybrid earthquakes that are brittle-failure events. Geophysical Research Letters, 34, L06308. https://doi.org/10.1029/2006GL028714

Henderson, J. R., Barton, D. J., & Foulger, G. R. (2002). Fractal clustering of induced seismicity in The Geysers geothermal area, California. Geophysical Journal International, 139(2), 317–324.

Holmgren, J. M., Atkinson, G. M., & Ghofrani, H. (2019). Stress drops and directivity of induced earthquakes in the western Canada sedimentary basin. Bulletin of the Seismological Society of America, 109(4), 1635–1652. https://doi.org/10.1785/0120190035

Huang, Y., et al. (2017). Stress drops of induced and tectonic earthquakes in the central United States are indistinguishable. Science Advances, 3, e1700772. https://doi.org/10.1126/sciadv.1700772

Hunt, T. M., & Latter, J. H. (1982). A survey of seismic activity near Wairakei geothermal field, New Zealand. Journal of Volcanology and Geothermal Research, 14(3–4), 319–334.

Ide, S., Beroza, G. C., Shelly, D. R., & Uchide, T. (2007). A scaling law for slow earthquakes. Nature, 447(7140), 76-79. https://doi.org/10.1038/nature05780
Istituto Nazionale di Geofisica e Vulcanologia (INGV). (2005). Rete Sismica Nazionale (RSN) [dataset]. Istituto Nazionale di Geofisica e Vulcanologia (INGV). https://doi.org/10.13127/SD/X0FXNH7QFY

Jousset, P., Haberland, C., Bauer, K., Árnason, K., Weber, M., & Fabriol, H. (2010). Seismic tomography and long-period earthquakes observation and

modeling at the Hengill geothermal volcanic complex, Iceland. In Proceedings World Geothermal Congress (pp. 25-29).

Kanamori, H. (1977). The energy release in great earthquakes. Journal of Geophysical Research, 82(20), 2981–2987. https://doi.org/10.1029/JB082i020p02981

Kanamori, H., & Brodsky, E. E. (2004). The physics of earthquakes. Reports on Progress in Physics, 67(8), 1429. https://doi.org/10.1088/0034-4885/67/8/R03

Kanamori, H., & Anderson, D. L. (1975). Theoretical basis of some empirical relations in seismology. Bulletin of the Seismological Society of America, 65(5), 1073–1095.

Klinger, A. G., & Werner, M. J. (2022). Stress drops of hydraulic fracturing induced microseismicity in the Horn River basin: Challenges at high frequencies recorded by borehole geophones. Geophysical Journal International, 228, 2018–2037. https://doi.org/10.1093/gji/ggab458

Köseoğlu, Y. (2013). A simple microwave-assisted combustion synthesis and structural, optical and magnetic characterization of ZnO nanoplatelets. Ceramics International, 39(8), 9225-9230. https://doi.org/10.1016/j.ceramint.2013.09.008

Latter, J.H., 1980, Volcanic earthquakes and their relationship to eruptions at Ruapehu and Ngauruhoe volcanoes: Journal of Volcanology and Geothermal Research, v.9, p. 293–309.
Lazzarotto, A., Costantini, A., Bossio, A., Foresi, L. M., Mazzei, R., & Salvatorini, G. (2002a). Carta Geologica d'Italia alla scala 1:50.000, Foglio n. 306 Massa Marittima. Servizio Geologico d'Italia, L.A.C., Firenze.

Madariaga, R. (1976). Dynamics of an expanding circular fault. Bulletin of the Seismological Society of America, 66(3), 639–666.

Malagnini, L., & Munafò, I. (2018). On the relationship between M_L and M_w in a broad range: An example from the Apennines, Italy. Bulletin of the Seismological Society of America, 108(2), 1018-1024. https://doi.org/10.1785/0120170303

Matoza, R. S., Shearer, P. M., & Okubo, P. G. (2014). High-precision relocation of long-period events beneath the summit region of Kılauea Volcano, Hawai'i, from 1986 to 2009. Geophysical Research Letters, 41(10), 3413–3421. https://doi.org/10.1002/2014gl059819

McNutt, S.R., 2002, Volcano seismology and monitoring for eruptions, chap. 25 of Lee, W.H.K., Kanamori, H, Jennings, P.C., and Kisslinger, C., eds,

International handbook of earthquake and engineering seismology: Academic Press, v. 81A.

Mignan, A., Landtwing, D., Kästli, P., Mena, B., & Wiemer, S. (2015). Induced seismicity risk analysis of the 2006 Basel, Switzerland, enhanced geothermal system project: Influence of uncertainties on risk mitigation. Geothermics, 53, 133–146.

Minissale, A. (1991). The Larderello geothermal field: A review. Earth-Science Reviews, 31(2), 133-151. https://doi.org/10.1016/0012-8252(91)90018-B

Mulyadi. (2010). Case study: hydraulic fracturing experiment in the Wayang Windu Geothermal field. In Proceedings of the World Geothermal Congress, Bali, Indonesia, 25–29 April 2010.

Musumeci, G., Bocini, L., & Corsi, R. (2002). Alpine tectonothermal evolution of the Tuscan Metamorphic Complex in the Larderello geothermal field (northern Apennines, Italy). Journal of the Geological Society, London, 159, 443-456. https://doi.org/10.1144/0016-764901-084

Neuberg, J. W., Tuffen, H., Collier, L., Green, D., Powell, T., & Dingwell, D. (2006). The trigger mechanism of low-frequency earthquakes on Montserrat. Journal of Volcanology and Geothermal Research, 153, 37–50. https://doi.org/10.1016/j.jvolgeores.2005.08.008

Pandeli, E., Elter, P., & Vittorio, S. (1994). Geological evolution of the Tuscan Nappe in the Larderello geothermal field (southern Tuscany, Italy). Journal of Structural Geology, 16(2), 287-304.

Paul, A., & Hazarika, D. (2022). Occurrences of low-stress drop earthquakes in the eastern Ladakh-Karakoram zone of the Trans Himalaya and their tectonic implications. Journal of Asian Earth Sciences: X, 7, 100080. https://doi.org/10.1016/j.jaesx.2022.100080

Pitt, A. M., & Hill, D. P. (1994). Long-period earthquakes in the Long Valley caldera region, eastern California. Geophysical Research Letters, 21, 1679.

Rafferty, J. P. (2024, June 10). Moment magnitude. Encyclopedia Britannica. https://www.britannica.com/science/moment-magnitude

Reid, H. F. (1910). The mechanics of the earthquake. In The California earthquake of April 18, 1906. Report of the State Earthquake Investigation Commission, Carnegie Institution, Washington, D.C., 192 pp.

Rovida, A., Locati, M., Camassi, R., Lolli, B., & Gasperini, P. (Eds.). (2016). CPTI15, the 2015 version of the Parametric Catalogue of Italian Earthquakes. Istituto Nazionale di Geofisica e Vulcanologia. http://doi.org/10.6092/INGV.IT-CPTI15

Saccorotti, G., Piccinini, D., Zupo, M., Mazzarini, F., Chiarabba, C., Piana Agostinetti, N., Licciardi, A., & Bagaglia, M. (2014). The deep structure of the Larderello-Travale geothermal field (Italy) from integrated, passive seismic investigations. Energy Procedia, 59, 227-234. https://doi.org/10.1016/j.egypro.2014.10.371

Scholz, C. H. (1990). The Mechanics of Earthquakes and Faulting. Cambridge University Press.

Shearer, P. M. (2009). Introduction to seismology (2nd ed.). Cambridge University Press.

Shelly, D. R., & Hardebeck, J. L. (2010). Precise tremor source locations and amplitude variations along the lower-crustal central San Andreas fault. Geophysical Research Letters, 37, L14301. https://doi.org/10.1029/2010GL043672

Shelly, D. R., Beroza, G. C., Ide, S., & Nakamula, S. (2006). Low-frequency earthquakes in Shikoku, Japan, and their relationship to episodic tremor and slip. Nature, 442(7099), 188–191.

Silitonga, T. H., Siahaan, E. E., & Suroso. (2005). A Poisson's ratio distribution from Wadati diagram as indicator of fracturing of Lahendong geothermal field, North Sulawesi, Indonesia. In Proceedings of the World Geothermal Congress 2005, Antalya, Turkey, 24–29 April.

Simiyu, S. M. (1999). Induced seismicity during interference tests at OW-719, Kenya. Journal of Geothermal Science, 28, 785–802.

Song, Z., Tan, Y. J., & Roman, D. C. (2023). Deep long-period earthquakes at Akutan Volcano from 2005 to 2017 better track magma influxes compared to volcano-tectonic earthquakes. Geophysical Research Letters, 50, e2022GL101987. https://doi.org/10.1029/2022GL101987

Stork, A. L., Verdon, J. P., & Kendall, J.-M. (2014). The robustness of seismic moment and magnitudes estimated using spectral analysis. Geophysical Prospecting, 62(4), 862-878. https://doi.org/10.1111/1365-2478.12134

Trifu, C. I. (Ed.). (2002). The Mechanism of Induced Seismicity. Pure and Applied Geophysics, 159(1–3), Topical Issue. Birkhäuser.

USGS. (June 27, 2024). Spectrogram of a possible long-period (LP) earthquake in Yellowstone, August 26, 2021, near Norris Geyser Basin. Retrieved June 27, 2024, from https://www.usgs.gov/media/images/speclpjpg

USGS. (June 27, 2024). Spectrogram of a possible long-period (LP) earthquake in Yellowstone, August 26, 2021, near Norris Geyser Basin. Retrieved June 27, 2024, from https://www.usgs.gov/media/images/spectypicalnewjpg

Villa, I. M., & Puxeddu, M. (1994). Geochronology of the Larderello geothermal area: New data and the problem of inherited ages. Journal of Geodynamics, 17(1-2), 23-46.

Wang, Q.-Y., Frank, W. B., Abercrombie, R. E., Obara, K., & Kato, A. (2023). What makes low-frequency earthquakes low frequency. Science Advances, 9(32), eadh368. https://doi.org/10.1126/sciadv.adh368

Ward, P. L. (1972). Microearthquakes: Prospecting tool and possible hazard in the development of geothermal resources. Geothermics, 1(1), 3-12.

Wu, Q., Chapman, M., & Chen, X. (2018). Stress-drop variations of induced earthquakes in Oklahoma. Bulletin of the Seismological Society of America, 108(3), 1107–1123. https://doi.org/10.1785/0120170335

Yamabe, T. H., & Hamza, V. M. (1996). Geothermal investigations in an area of induced seismic activity, Northern Sao Paulo State, Brazil. Tectonophysics, 253, 209–225.

Zastrow, M. 2019. South Korea accepts geothermal plant probably caused destructive quake. Nature. https://doi.org/10.1038/d41586-019-00959-4.

Acknowledgement

I am grateful to Prof. Piero Poli for his guidance, encouragement, and support throughout this research. His expertise and thoughtful feedback have been instrumental in shaping this study. I also want to thank Prof. Giulio Di Toro for his assistance and valuable insights during this work. I couldn't have completed this thesis without them.